phys. stat. sol. (c) **1**, No. 8, 2003–2027 (2004) / **DOI** 10.1002/pssc.200404761

Advances in the theory of electronic structure of semiconductors

Jacek A. Majewski[*], **Stefan Birner, Alex Trellakis, Matthias Sabathil,** and **Peter Vogl**

Walter Schottky Institut, Technische Universität München, Am Coulombwall, 85748 Garching, Germany

Received 15 March 2004, revised 22 April 2004, accepted 27 April 2004
Published online 2 June 2004

PACS 71.15–m, 71.15.Mb, 71.20.Nr, 73.21.–b

This paper reviews the present status of recently developed ab-initio as well as semiempirical electronic structure methods that are particularly suited for semiconductors and mesoscopic semiconductor structures. In assessing each method, we provide some additional and hitherto unpublished details about its implementation. In the first part of the paper, we discuss two important extensions of the local density functional theory, the screened-exchange and the exact exchange method namely. We proceed with a discussion of the relativistic local density method that is essential for a prediction of spin-related phenomena in semiconductors. Finally, we review a rather complete and extensve implementation of the envelope function approach for arbitrary three-dimensional nanometer device structures.

© 2004 WILEY-VCH Verlag GmbH & Co. KGaA, Weinheim

1 Introduction

The quickly progressing technology of semiconductor quantum structures requires and depends on reliable predictive theoretical methods for systematically improving, designing, and understanding the electronic and optical properties of such structures. In this paper we will review the present status of some major electronic structure methods for a wide variety of mesoscopic semiconductor structures at or close to thermodynamic equilibrium. Since this work is published as a final report of a center of excellence, we will primarily focus on methods that we have developed or at least contributed to in the context of semiconductor devices. To develop electronic structure methods methods for nanodevices is an extremely challenging task. First of all, even the smallest semiconductor quantum structure such as a single quantum dot contains hundreds of thousands of atoms. Since the most accurate theoretical electronic structure methods are based on a microsocopic description that includes the details of each atom, such methods cannot be applied directly to mesoscopic systems. Secondly, such structures are often not in thermodynamical equilibrium, but are biased and contain considerable carrier concentrations that add long-range potentials to the nano-scale periodic crystal potential. These problems can only be tackled within continuum approaches that interpolate carefully between the microscopic physics and macroscopic descriptions. While there are many electronic structure methods that are optimized to some material class and length scale, there is obviously none without problems and significant weaknesses. In this review, we will start with several ab-initio methods that have been developed or optimized for semiconductors, provide illustrative examples, and then discuss the adaptation of continuum theories bases on the envelope function theory to semiconductor nanostructures.

[*] Corresponding author: e-mail: majewski@wsi.tum.de, Phone: +49 89 289 12750, Fax: +49 89 289 12737

© 2004 WILEY-VCH Verlag GmbH & Co. KGaA, Weinheim

The reader may wonder why this paper does not discuss the ocean of methods that lie between ab-initio and continuum models, such as empirical tight binding [1] or empirical pseudopotential methods [2], even though both methods have shown to be capable of dealing with systems that consist of up to one million atoms. The problem with these intermediate methods is their limited predictive power, their limited generality, and their computational effort that lies annoyingly close to that of ab-initio methods. While these methods undoubtedly play an important and useful role for many problems, we believe that continuum approaches with parameters that have been determined by ab-initio methods are most suitable for semiconductor quantum devices.

Ab-initio methods have proven exceedingly useful for predictions of physical properties of molecules or periodic systems with unit cells of no more than a few hundred atoms [3]. In addition, they can provide reliable parameters for continuum approaches. Most ab-initio calculations for semiconductor structures have been and are being performed within the local density approximation (LDA) [4] or the generalized gradient approximation (GGA) [5, 6] to density functional theory [7]. Unfortunately, both of these methods are plagued by the so-called "band gap problem"; they predict band gaps in bulk semiconductors that are way too small. Associated with this problem, one finds that effective masses are often significantly underestimated as well, which then shows up in optical properties etc. One remedy is to correct an LDA calculation a posteriori by calculating quasiparticle self-energies in terms of the so-called GW method [8, 9]. In this review, we will discuss two fully self-consistent schemes that both lead to much improved band gaps and simultaneously predict satisfactory structural properties of semiconductors. These methods have been called screened-exchange LDA (sX-LDA) [10, 11] and the exact exchange method (EXX) [12], respectively.

In the context of quantum devices, spin phenomena in semiconductors have become particularly important. We have developed and refined LDA based ab-initio calculations that are based on relativistic pseudopotentials and include the spin-orbit interaction nonperturbatively. We will therefore review these developments and demonstrate their accuracy by discussing spin splitting in semiconductors and heterostructures.

Finally, we will turn to mesoscopic systems. Based on the envelope function approach, and making use of results obtained with the ab-initio methods, we have developed a program package that allows one to study the electronic structure and optical properties of basically arbitrarily shaped three-dimensional semiconductor nano-structures and optoelectronic nano-devices. This package, termed nextnano^3 is also discussed together with illustrative examples.

The paper is organized as follows. In Sec. 2 the theoretical basis of the two realizations of the density functional theory beyond the LDA are presented. The examples of practical applications of these schemes in semiconductors demonstrate superiority of these approaches in comparison to the standard LDA method. New developments allowing to investigate efficiently the relativistic effects in the band structure of semiconductors are sketched in Sect. 3. The electronic structure methods for mesoscopic systems are discussed in Sec. 4.

2 Methods with new density functionals

In density functional theory, the standard Kohn–Sham-equations for one particle orbitals ϕ_i and energies ε_i read [4]

$$[-\tfrac{1}{2}\nabla^2 + v_{\text{ext}}(\boldsymbol{r}) + u(\boldsymbol{r}) + v_x(\boldsymbol{r}) + v_c(\boldsymbol{r})]\,\phi_i(\boldsymbol{r}) = \varepsilon_i \phi_i(\boldsymbol{r})\,, \tag{1}$$

where $v_{\text{ext}}(\boldsymbol{r})$ is the external potential, $v_x(\boldsymbol{r}) = \dfrac{\delta E_x[\rho]}{\delta\rho(\boldsymbol{r})}$ and $v_c(\boldsymbol{r}) = \dfrac{\delta E_c[\rho]}{\delta\rho(\boldsymbol{r})}$ are the exchange and correlation potential, respectively. The local potential $v_x(\boldsymbol{r})$ and $v_c(\boldsymbol{r})$ are functional derivatives of the exchange energy and correlation energy functional with respect to the one-particle densities, respectively. The correlation energy functional $E_c[\rho]$ is generally unknown and must be approximated in any implementation of density functional theory. Within the LDA and GGA methods, both the exchange functional $E_x[\rho]$ and the correlation energy are approximated by expressions that are derived from the homogeneous electron gas.

© 2004 WILEY-VCH Verlag GmbH & Co. KGaA, Weinheim

Here we discuss two alternative approaches to LDA or GGA. In one case, one derives single-particle equations from a nonlocal functional, invoking the idea that it may be simpler to find adequate approximations to the nonlocal electron–electron interaction rather than to find an accurate local density functional. Indeed, the Hartree–Fock method is such an example. This approach has originally been proposed by Kleinman and Bylander [10] and has been termed screened-exchange (sX-LDA) method. Secondly, we discuss a method that is based on the Kohn–Sham equations but eliminates one of the two approximations in this scheme: the local exchange potential $v_x(\boldsymbol{r})$ is calculated exactly. This procedure has been termed exact exchange method [12].

2.1 Screened, nonlocal exchange method

This method belongs to the class of generalized Kohn–Sham schemes (GKS) where non-local (Hartree–Fock like) potentials are included in the single-particle equations. This method has been originally developed in Ref. [10]. Seidl et al. [11] have proven that this method is a rigorous density functional theory that is protected by a minimization principle, developed it further and applied it to semiconductors. Here we review the basic principle of this approach that has recently been implemented in a commercial software [13].

Let us denote by E_x^{sx} a statically screened exchange interaction with the Thomas–Fermi screening constant k_{TF},

$$E_x^{sx} = -\sum_{i<j}^{N} \int \mathrm{d}\boldsymbol{r}\, \mathrm{d}\boldsymbol{r}' \, \frac{\phi_i^*(\boldsymbol{r})\, \phi_j^*(\boldsymbol{r}')\, \mathrm{e}^{-k_{\mathrm{TF}}|\boldsymbol{r}-\boldsymbol{r}'|}\, \phi_j(\boldsymbol{r})\, \phi_i(\boldsymbol{r}')}{|\boldsymbol{r}-\boldsymbol{r}'|} \,. \tag{2}$$

The basic idea of the method is to calculate the screened nonlocal electron–electron interaction exactly and treat all remaining terms in the total energy functional within LDA. The resulting generalized Kohn–Sham equations (*sX-LDA equations*) take the form

$$[-\tfrac{1}{2}\nabla^2 + v(\boldsymbol{r}) + u([\rho];\boldsymbol{r}) + v_x^{sx}([\rho];\boldsymbol{r}) + v_c([\rho];\boldsymbol{r})]\, \phi_i(\boldsymbol{r}) - \int \mathrm{d}\boldsymbol{r}'\, v_x^{sx,\mathrm{NL}}(\boldsymbol{r},\boldsymbol{r}')\, \phi_i(\boldsymbol{r}') = \varepsilon_i \phi_i \,, \tag{3}$$

$$v_x^{sx,\mathrm{NL}}(\boldsymbol{r},\boldsymbol{r}') = -\sum_{j=1}^{N} \frac{\phi_j(\boldsymbol{r})\, \mathrm{e}^{-k_{\mathrm{TF}}|\boldsymbol{r}-\boldsymbol{r}'|}\, \phi_j^*(\boldsymbol{r}')}{|\boldsymbol{r}-\boldsymbol{r}'|} \,, \tag{4}$$

where $\hat{v}_x^{sx,\mathrm{NL}}$ is the nonlocal screened exchange operator, $u([\rho];\boldsymbol{r})$ is the electrostatic Hartree potential, and $v_x^{sx}([\rho];\boldsymbol{r})$ is the functional derivative of $\tilde{E}_x^{sx}[\rho] = E_x[\rho] - E_x^{sx}[\rho]$ with respect to the density. The functional $\tilde{E}_x^{sx}$ maybe approximated by LDA as follows

$$E_x[\rho] \simeq E_x^{\mathrm{LDA}}[\rho] = \int \mathrm{d}\boldsymbol{r}\, \rho(\boldsymbol{r})\, \epsilon_x[\rho] \,, \tag{5}$$

$$E_x^{sx}[\rho] \simeq E_x^{sx,\mathrm{LDA}}[\rho] = \int \mathrm{d}\boldsymbol{r}\, \rho(\boldsymbol{r})\, \epsilon_{sx}[\rho] \,, \tag{6}$$

with [14]

$$\epsilon_x[\rho] = -\frac{3}{4}\left(\frac{3}{\pi}\right)^{1/3} \rho^{1/3} \,, \tag{7}$$

$$\epsilon_{sx}[\rho] = -\frac{3}{4}\left(\frac{3}{\pi}\right)^{1/3} \rho^{1/3} F(z) \,, \tag{8}$$

$$F(z) = 1 - \frac{4}{3} z \arctan\frac{2}{z} - \frac{z^2}{6}\left[1 - \left(\frac{z^2}{4} + 3\right) \ln\left(1 + \frac{4}{z^2}\right)\right] . \tag{9}$$

Here, $z = k_{\mathrm{TF}}/\bar{k}_F$ and $\bar{k}_F$ is the Fermi wave vector corresponding to the average density. Thus, these energy contributions are approximated by functionals corresponding to the homogeneous electron gas.

© 2004 WILEY-VCH Verlag GmbH & Co. KGaA, Weinheim

2.1.1 Band gaps and structural properties in sX-LDA

This screened-exchange (sX-LDA) scheme has been implemented and used to study electronic and structural properties of several semiconductors [11]. The computations have been performed in the framework of the plane-wave pseudopotential method [15, 16], employing the *ab initio* norm conserving semilocal pseudopotentials of Bachelet, Hamann and Schlüter (BHS) [17]. The numerically most demanding part is the computation of the plane-wave matrix elements of the nonlocal exchange operator.

Figure 1 shows a significant increase in the calculated principal sX-LDA band gaps of Si, Ge, GaAs, InP and InSb compared to LDA results that have been obtained with the same BHS pseudopotentials and with the same experimental lattice constants. For materials that contain heavier anions (Ge, GaAs, and especially InSb), the spin-orbit interactions cannot be neglected. It is well established that the spin-orbit effects can be added perturbatively *a posteriori* in the LDA-pseudopotential framework. Consequently, we have simply decreased the calculated non-relativistic gaps by one third of the experimental valence band spin-orbit splitting at Γ ($\frac{1}{3}\Delta_0$). The resulating energy gaps between the lowest conduction band states in Γ, X, and L points and the top of the valence band and the valence band widths are summarized in Table 1.

We note that both Ge and InSb bulk semiconductors turn out to be metallic within the LDA. In InSb, even nonrelativistic LDA calculations that use pseudopotentials [18, 20] or the linearized augmented plane wave method [20] predict a *negative* gap at Γ, whereas the present non-relativistic sX-LDA procedure gives a *positive* gap of 0.495 eV. Taking the experimental value for the spin-orbit splitting in InSb, one obtains an sX-LDA band gap of 0.23 eV that perfectly matches the experimental band gap of 0.235 eV. Table 1 and Fig. 2 illustrate the significant overall improvement of the predicted band gaps throughout the Brillouin zone by the sX-LDA method. Generally the sX-LDA method predicts energy gaps in similarly good agreement with experiment as the *GW* method does but it additionally yields total energies and is fully self-consistent. There is a remaining minor problem with the semiconductor Ge that is incorrectly predicted to be a direct gap material but one cannot exclude this to be an artefact of the pseudopotential employed.

Table 2 displays the calculated structural properties of various bulk semiconductors as obtained by the sX-LDA method. The relative errors in the lattice constants a are below 0.5%, when compared to experiment. Since these errors are so small, we have calculated all energy gaps at the experimental lattice constants. The effect of zero point motion of the ions on a is one order of magnitude smaller than the remaining discrepancies between theory and experiment and has been neglected. Table 2 also shows that the bulk moduli predicted by sX-LDA underestimate the experimental values by typically 20%, and agree less well with experiment than the standard LDA results.

All the results discussed in this subsection have been obtained with the Thomas-Fermi (TF) dielectric function, using the valence electron density in the screening constant k_{TF}. Several alternative

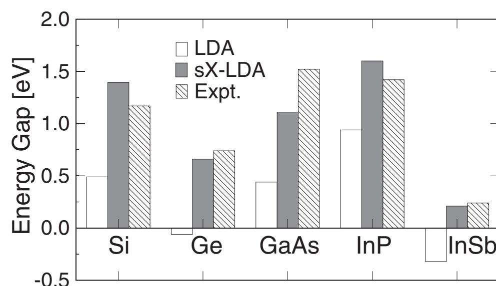

Fig. 1 Fundamental energy gaps in Si, Ge, GaAs, InP, and InSb calculated in sX-LDA method compared to the LDA and experimental values.

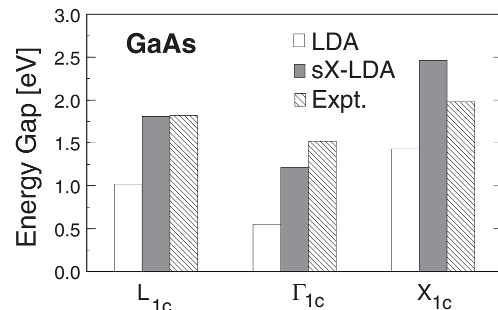

Fig. 2 Direct (Γ_{1c}) and indirect (L_{1c} and X_{1c}) energy gaps, relative to the valence band top, in GaAs calculated in sX-LDA method compared to the LDA and experimental values.

© 2004 WILEY-VCH Verlag GmbH & Co. KGaA, Weinheim

Table 1 Energy gaps between the lowest conduction states and the valence band edge and valence band widths (VBW) of Si, Ge, GaAs, InP, and InSb from present sX-LDA with Thomas-Fermi screening and LDA calculations compared to available experimental results taken from Ref. [21] except where noted. Energies are in eV.

	Si	Ge	GaAs	InP	InSb
$E(\Gamma)$	3.37	0.28	1.11	1.60	0.21
$E^{\mathrm{LDA}}(\Gamma)$	2.54	−0.06	0.44	0.94	−0.32
$E^{\mathrm{exp}}(\Gamma)$	3.05(1), 3.4	0.89	1.52	1.42	0.24
$E(X)$	1.55	1.45	2.35	2.75	1.82
$E^{\mathrm{LDA}}(X)$	0.61	0.61	1.32	1.64	1.06
$E^{\mathrm{exp}}(X)$	1.25(1)	1.3 ± 0.2	1.98	2.38	1.79
$E(L)$	2.18	0.66	1.70	2.45	1.02
$E^{\mathrm{LDA}}(L)$	1.44	0.07	0.91	1.56	0.35
$E^{\mathrm{exp}}(L)$	1.65 ± 0.01 2.1, 2.4 ±0.15(2)	0.74	1.81	2.03	–
VBW	12.47	13.41	13.40	11.91	11.02
$\mathrm{VBW}^{\mathrm{LDA}}$	11.94	12.80	12.40	11.20	10.48
$\mathrm{VBW}^{\mathrm{exp}}$	12.5 ± 0.6	12.6,12.9 ± 0.3(3)	13.1	11.0	11.7, 11.2(4)

(1) – Ref. [22], (2) – Ref. [23], (3) – Ref. [24], (4) – Ref. [25]

screening models have been also tested [11] but lead to very similar results. We note that the sX-LDA method has recently been implemented in the framework of the linearized augmented plane wave method (LAPW) and successfully applied to a broad spectrum of bulk materials [13, 29]. More recent implementations employ more accurate screening models [30].

2.2 Exact exchange Kohn–Sham formalism

We now turn to another density functional method, named EXX, that allows one to treat the exchange interaction in solids exactly and has been proposed in Ref. [31]. In this method, only local potentials enter the single-particle Kohn–Sham equations. It has been used to calculate lattice constants, cohesive energies, Kohn–Sham eigenvalues, dielectric functions, and effective masses of various zincblende semiconductors. Interestingly, all of these quantities turn out to be in very good agreement with experiment. From a theoretical point of view, the EXX method cures a principal weakness of LDA, namely the spurious self-interaction that is caused by an incomplete cancellation of the Hartree interaction and the approximate LDA exchange functional. This unphysical self interaction leads to a

Table 2 Theoretical lattice constants (in Å) and bulk moduli (in GPa), both obtained from fit to Murnaghan's equation of state [26], of Si, Ge, GaAs, and InP in sX-LDA with Thomas–Fermi screening. Experimental values are from Refs. [21] and [27].

	Si	Ge	GaAs	InP
a_0	5.421	5.635	5.627	5.776
a_0^{LDA}	5.37(1)	5.567(1)	5.51(1)	5.74(2)
a_0^{exp}	5.43	5.657	5.652	5.869
B_0	89.3	62.7	63.1	65.5
B_0^{LDA}	96.8(1)	76.2(1)	77.8(1)	76.0(2)
B_0^{exp}	87.6–97.9	73.4–75.8	75.3–76.9	72.5

(1) – Ref. [28], (2) – Ref. [20]

© 2004 WILEY-VCH Verlag GmbH & Co. KGaA, Weinheim

self-repulsion which pushes up all occupied bands but does not affect the empty ones. As a consequence, the energy gap is underestimated in LDA. In addition, this self-repulsion leads to much too shallow excited states in atoms and molecules. The EXX method treats the exchange energy exactly and thus cures, in a systematic way, this notorious problem of DFT and guarantees a correct asymptotic ($r \to \infty$) behavior of the Kohn–Sham potential.

The exact exchange energy functional in the Kohn–Sham approach is given by

$$E_x[\rho] = -\frac{e^2}{2}\sum_{ij}^{occ}\int\int \mathrm{d}\boldsymbol{r}\,\mathrm{d}\boldsymbol{r}'\,\frac{\varphi_i^*(\boldsymbol{r})\,\varphi_i(\boldsymbol{r}')\,\varphi_j(\boldsymbol{r}')\,\varphi_j^*(\boldsymbol{r})}{|\boldsymbol{r}-\boldsymbol{r}'|}\,. \tag{10}$$

$E_x[\rho]$ is implicitly a functional of density, but explicitly only its dependence on the set of occupied Kohn–Sham orbitals is known. Thus, it is not straightforward to calculate the corresponding exchange potential $v_x(\boldsymbol{r}) = \frac{\delta E_x[\rho]}{\delta\rho(\boldsymbol{r})}$. For free atoms, this goal has been already achieved for many years by what is known as the optimized effective potential (OEP) method [32]. In that case, the exchange potential is obtained from an integral equation. The OEP formalism was originally meant to approximate the Hartree–Fock method by constructing a local potential whose eigenfunctions minimize the expectation value of the Hartree–Fock Hamiltonian. Only later it has been recognized that such an approach represents an exact exchange-only Kohn–Sham method within density-functional theory [12]. Unfortunately, due to its complexity, the original OEP scheme is only applicable to one-dimensional systems with spherical symmetry. A straightforward generalization of the OEP scheme for solids is not possible. Nevertheless, several approximate approaches have been developed to extend this method to solids. One approach used a spherical shape approximation for the potential and treated the ion cores nonrelativistically [33–37]. The second approach approximated the one-particle Green function by replacing some eigenvalue differences by a constant [38, 39]. The latter approximation – known as the KLI method – was shown to affect the OEP results for atoms only negligibly [38, 40, 41]. Importantly, both schemes gave encouraging results for band structures in semiconductors and insulators [37, 39, 42–44].

In a series of papers, Görling and others [31, 45–48], including some of the authors of this review, have been able to show that the exact exchange potential $v_x(\boldsymbol{r})$ for three dimensional systems can be rigorously expressed in terms of linear response functions of the noninteracting system [31, 45–48]. Based on this approach, that will be detailed below, solid state calculations have become possible. Very recently, it has been shown that the exact OEP potential for a crystal may be constructed iteratively from the first order shifts of the Kohn–Sham orbitals [49, 50]. This new method appears to be simpler that the former one [31, 45–48] as it does not require one to sum over the unoccupied Kohn–Sham states nor to invert the response matrix. However, this method has been applied only for atoms and sodium clusters up to now [50]. In the following, we detail the main points of the construction of the $v_x(\boldsymbol{r})$ in terms of the EXX method [31] and discuss some applications.

2.2.1 Theory

The difficulty in calculating the exact $V_x(\boldsymbol{r})$ lies in the fact that $E_x[\rho]$ in Eq. (10) is explicitly known only in terms of the Kohn–Sham orbitals but not in terms of the density $\rho(\boldsymbol{r})$. Nevertheless, this functional derivative can be determined explicitly by noting that it is sufficient to determine the infinitesimal (first order) change in the exchange energy, $\delta E_x[\rho]$, with respect to an infinitesimal (charge-conserving) change $\delta\rho(\boldsymbol{r})$ in the density. The central idea of the EXX method [51] is to split the functional derivative in $v_x(\boldsymbol{r}) = \frac{\delta E_x[\rho]}{\delta\rho(\boldsymbol{r})}$ into separate terms each of which can be calculated exactly. By employing the chain rule, we can write

$$V_x(\boldsymbol{r}) = \frac{\delta E_x[\rho]}{\delta\rho(\boldsymbol{r})} = \sum_{v\boldsymbol{k}}\int \mathrm{d}\boldsymbol{r}'\int \mathrm{d}\boldsymbol{r}''\left[\frac{\delta E_x[\rho]}{\delta\varphi_{v\boldsymbol{k}}(\boldsymbol{r}')}\,\frac{\delta\varphi_{v\boldsymbol{k}}(\boldsymbol{r}')}{\delta V_{\mathrm{KS}}(\boldsymbol{r}'')} + \mathrm{c.c.}\right]\frac{\delta V_{\mathrm{KS}}(\boldsymbol{r}'')}{\delta\rho(\boldsymbol{r})}\,. \tag{11}$$

© 2004 WILEY-VCH Verlag GmbH & Co. KGaA, Weinheim

In Eq. (11) and in what follows, we have used a notation that is suitable for solids; We denote the occupied and empty states as valence ($v\boldsymbol{k}$) and conduction ($c\boldsymbol{k}$) states of given Bloch vector $\boldsymbol{k}$, respectively. All three functional derivatives on the right hand side of Eq. (11) may be calculated directly as will be outlined below. The first one is obtained by straightforward differentiation of $E_x[\rho]$ in Eq. (10) and reads

$$\frac{\delta E_x[\rho]}{\delta \varphi_{v\boldsymbol{k}}(\boldsymbol{r}')} = -e^2 \sum_{v'\boldsymbol{k}'} \int \mathrm{d}\boldsymbol{r}_1 \, \frac{\varphi^*_{v'\boldsymbol{k}'}(\boldsymbol{r}') \, \varphi^*_{v\boldsymbol{k}}(\boldsymbol{r}_1) \, \varphi_{v'\boldsymbol{k}'}(\boldsymbol{r}_1)}{|\boldsymbol{r}_1 - \boldsymbol{r}'|} \, . \tag{12}$$

The second one is the first order change in the Kohn–Sham orbitals induced by an infinitesimal change in the Kohn–Sham potential. In analogy to first order perturbation theory, one obtains

$$\frac{\delta \varphi_{v\boldsymbol{k}}(\boldsymbol{r}')}{\delta V_{\mathrm{KS}}(\boldsymbol{r}'')} = \sum_{n'\boldsymbol{k}' \neq v\boldsymbol{k}} \varphi_{n'\boldsymbol{k}'}(\boldsymbol{r}') \, \frac{\varphi^*_{n'\boldsymbol{k}'}(\boldsymbol{r}'') \, \varphi_{v\boldsymbol{k}}(\boldsymbol{r}'')}{\varepsilon_{v\boldsymbol{k}} - \varepsilon_{n'\boldsymbol{k}'}} \, . \tag{13}$$

Insertion of Eqs. (12) and (13) into (11) leads to

$$V_x(\boldsymbol{r}) = \int \mathrm{d}\boldsymbol{r}' \sum_{vc\boldsymbol{k}} \left[\langle v\boldsymbol{k}| \, \hat{V}_x^{\mathrm{NL}} \, |c\boldsymbol{k}\rangle \, \frac{\varphi^*_{c\boldsymbol{k}}(\boldsymbol{r}') \, \varphi_{v\boldsymbol{k}}(\boldsymbol{r}')}{\varepsilon_{v\boldsymbol{k}} - \varepsilon_{c\boldsymbol{k}}} + \text{c.c.} \right] \frac{\delta V_{\mathrm{KS}}(\boldsymbol{r}')}{\delta \rho(\boldsymbol{r})} \, , \tag{14}$$

where $\langle \boldsymbol{r} \,|\, c\boldsymbol{k}\rangle = \varphi_{c\boldsymbol{k}}(\boldsymbol{r})$ are the unoccupied conduction band Kohn–Sham orbitals. Note that the non-local operator $\hat{V}_x^{\mathrm{NL}}$ has the same form as the Hartree–Fock exchange operator but is built of Kohn–Sham rather than of Hartree–Fock orbitals. In real space, it is an integral operator with the kernel

$$V_x^{\mathrm{NL}}(\boldsymbol{r}, \boldsymbol{r}') = -e^2 \sum_{v\boldsymbol{q}} \frac{\varphi_{v\boldsymbol{q}}(\boldsymbol{r}) \varphi^*_{v\boldsymbol{q}}(\boldsymbol{r}')}{|\boldsymbol{r} - \boldsymbol{r}'|} , \tag{15}$$

whereas it reads in reciprocal space

$$V_x^{\mathrm{NL}}(\boldsymbol{k}, \boldsymbol{G}, \boldsymbol{G}') = -\frac{4\pi e^2}{\Omega} \sum_{v\boldsymbol{q}\boldsymbol{G}_1} \frac{C_{v\boldsymbol{q}}(\boldsymbol{G} + \boldsymbol{G}_1) \, C^*_{v\mathbf{q}}(\boldsymbol{G}' + \boldsymbol{G}_1)}{|\boldsymbol{q} - \boldsymbol{k} + \boldsymbol{G}_1|^2} \, , \tag{16}$$

where $\boldsymbol{G}, \boldsymbol{G}', \boldsymbol{G}_1$ denote reciprocal lattice vectors, $C_{v\boldsymbol{q}}(\boldsymbol{G}) = \langle \boldsymbol{q} + \boldsymbol{G} \,|\, v\boldsymbol{q}\rangle$ is the plane wave expansion coefficients of the Bloch function $|v\boldsymbol{q}\rangle$ associated with $\boldsymbol{G}$, and Ω is the crystal volume. The third remaining functional derivative in Eq. (11) is the first order change in the Kohn–Sham potential induced by a small change in the density. In order to calculate it, it is easier to consider the inverse functional derivative since it can be obtained from linear response theory of independent particles and we determine this quantity first. One has

$$\frac{\delta \rho(\boldsymbol{r})}{\delta V_{\mathrm{KS}}(\boldsymbol{r}')} = \chi_0(\boldsymbol{r}, \boldsymbol{r}') \, ,$$
$$\chi_0(\boldsymbol{r}, \boldsymbol{r}') = 2 \sum_{vc\boldsymbol{k}} \frac{\varphi^*_{v\boldsymbol{k}}(\boldsymbol{r}) \, \varphi_{c\boldsymbol{k}}(\boldsymbol{r}) \, \varphi^*_{c\boldsymbol{k}}(\boldsymbol{r}') \, \varphi_{v\boldsymbol{k}}(\boldsymbol{r}') + \text{c.c.}}{\varepsilon_{v\boldsymbol{k}} - \varepsilon_{c\boldsymbol{k}}} \, . \tag{17}$$

We require that a first order change in the Kohn–Sham potential always induces a change in the density that is also of first order. In this case, the Hohenberg-Kohn theorem guarantees a one-to-one mapping [51] between $\delta\rho(\boldsymbol{r})$ and $\delta V_{\mathrm{KS}}(\boldsymbol{r})$. However, this mapping excludes constant potential changes since a rigid potential shift has no effect on the wave functions and the density. With Eq. (17), this implies that one has

$$\int \mathrm{d}\boldsymbol{r}' \, \chi_0(\boldsymbol{r}, \boldsymbol{r}') = 0 \, . \tag{18}$$

© 2004 WILEY-VCH Verlag GmbH & Co. KGaA, Weinheim

Thus, the mapping χ_0 cannot be inverted and we need to consider a restricted function space that excludes constant changes of the KS potential. This is most easily achieved through a Fourier expansion which leads to [52]

$$\delta\rho(\boldsymbol{G}) = \sum_{\boldsymbol{G}'} \chi_0(\boldsymbol{G},\boldsymbol{G}')\,\delta V_{\mathrm{KS}}(\boldsymbol{G}') \,,$$
$$\chi_0(\boldsymbol{G},\boldsymbol{G}') = \frac{4}{\Omega} \sum_{vc\boldsymbol{k}} \frac{\langle v\boldsymbol{k}|\,\mathrm{e}^{-i\boldsymbol{G}\boldsymbol{r}}\,|c\boldsymbol{k}\rangle\;\langle c\boldsymbol{k}|\,\mathrm{e}^{i\boldsymbol{G}'\boldsymbol{r}}\,|v\boldsymbol{k}\rangle}{\varepsilon_{v\boldsymbol{k}} - \varepsilon_{c\boldsymbol{k}}} \,. \qquad (19)$$

All charge conserving changes in the density lie within the sub-space $\boldsymbol{G} \neq \boldsymbol{0}$. In addition, the sub-space $\boldsymbol{G}' \neq \boldsymbol{0}$ excludes all constant potential changes. Therefore, the sub-matrix of χ_0 with both $\boldsymbol{G}$ and $\boldsymbol{G}' \neq \boldsymbol{0}$ – that we denote by $\tilde{\chi}_0$ – is regular and can be inverted unambiguously. After a straightforward transformation of Eq. (14) to reciprocal lattice space, we arrive at the following exact expression for the exchange potential in Eq. (14),

$$V_x(\boldsymbol{G}) = \sum_{\boldsymbol{G}'\neq 0} [E(\boldsymbol{G}') + E^*(-\boldsymbol{G}')]\,\tilde{\chi}_0^{-1}(\boldsymbol{G},\boldsymbol{G}') \,,$$
$$E(\boldsymbol{G}) = \frac{2}{\Omega} \sum_{vc\boldsymbol{k}} \frac{\langle v\boldsymbol{k}|\,\hat{V}_x^{\mathrm{NL}}\,|c\boldsymbol{k}\rangle\;\langle c\boldsymbol{k}|\,\mathrm{e}^{-i\boldsymbol{G}\boldsymbol{r}}\,|v\boldsymbol{k}\rangle}{\varepsilon_{v\boldsymbol{k}} - \varepsilon_{c\boldsymbol{k}}} \,. \qquad (20)$$

In a self-consistent Kohn–Sham calculation, both quantities $\tilde{\chi}_0(\boldsymbol{G},\boldsymbol{G}')$ and $E(\boldsymbol{G})$ in Eq. (20) have to be updated in each step of the iteration cycle. For a system with inversion symmetry, one has $E^*(-\boldsymbol{G}) = E(\boldsymbol{G})$. The present formalism does not yield the spatial average of the exchange potential, i.e. its $\boldsymbol{G} = \boldsymbol{0}$ component. Indeed, exchange-correlation potentials are defined only up to an additive constant in the Kohn–Sham formalism with fixed particle number. $V_x(\boldsymbol{G} = 0)$ does not enter the total energy or eigenvalue differences and may be set to zero without loss of generality.

By construction, the exact exchange energy cancels the self-interaction contributions in the Hartree energy. Therefore, a calculation of the exact exchange potential Eq. (20) yields a realization of Kohn–Sham theory that is rigorously self-interaction free, in contrast to the LDA and GGA. In addition, expression Eq. (20) satisfies all scaling relations and asymptotic convergence laws that are known for the Kohn–Sham exchange potential [53, 54]. Even though Eqs. (14) and (20) show that the value of $V_x(\boldsymbol{r})$ at any point $\boldsymbol{r}$ depends on the Kohn–Sham wave functions and eigenvalues in the whole unit cell, the locality of the exchange potential significantly simplifies band structure calculations, since it is independent of the Bloch wave vector.

We would like to emphasize that there is an important conceptual difference between the EXX exchange scheme and Hartree–Fock. In the Hartree–Fock formalism, the single particle equations contain a *nonlocal* exchange potential, and they provide an approximate solution of the many electron problem. By contrast, the EXX formalism leads to a *local* exchange potential and provides, in principle, an exact solution of the many-body problem if it is augmented by the exact correlation potential. Finally, we point out that the procedure outlined in Eqs. (11)–(20) can be applied not only to the Kohn–Sham realization of density functional theory but also to generalized Kohn–Sham schemes as described in the previous subsection; the present procedure allows one to take the functional derivative of any orbital dependent expression with respect to the electron density.

2.2.2 EXX pseudopotentials

The EXX scheme has been implemented for solids in the framework of the plane wave pseudopotential formalism. This brings up an additional problem, namely the issue of consistency between the atomic pseudopotentials and the calculation of the valence electron energy functional in the solid. Within LDA, the construction of ab-initio ionic pseudopotentials is well established and straightforward [55]. The construction of EXX pseudopotentials, on the other hand, is far from being trivial [56, 57]. Here we would like to summarize the main points that are needed to construct EXX-pseudopotentials.

© 2004 WILEY-VCH Verlag GmbH & Co. KGaA, Weinheim

The starting point for the generation of norm-conserving EXX pseudopotentials are relativistic exact-exchange (REXX) calculations for atoms [58–60]. The resulting REXX equations are valid for arbitrary open shell systems with a non-spherical electron density $\rho(\boldsymbol{r})$. In this form, however, they are not well adapted to the construction of transferable pseudopotentials. "Good" pseudopotentials describe the interaction of extended valence states with a closed-shell ion core and should not depend on the detailed valence electron configuration they are embedded into. Therefore, it is necessary to employ an appropriate symmetrization scheme that transforms the open-shell atoms into species with spherical symmetry, characterized by a spherical electronic density $\rho(r)$ and a spherical Kohn–Sham potential $v_s(r)$. This can been achieved by performing generalized configuration-averaging procedure that eliminates the explicit dependence of the Kohn–Sham potential on atomic subshells [56]. Such a procedure yields the one electron energies ϵ_{nlj} and radial two-component spinors $(f_{nlj}, g_{nlj})^\top$, where n is the main quantum number, j is the component of the total-angular-momentum, and l is the spatial angular momentum quantum number. The calculation of ϵ_{nlj} and $(f_{nlj}, g_{nlj})^\top$ for the ground state of the neutral atom is the first step in the generation of the pseudopotential. In the next step, one constructs the pseudo-wave functions φ_{lj} for the valence electrons. Beyond the cutoff radius r_c^l, one sets them equal to the large component of the corresponding all-electron wave function, $\varphi_{lj}^{\text{ps}}(r) = f_{lj}(r)$. Within the core radius, one assumes nodeless functions, following reference [55] for standrad pseudopotentials. In addition, one requires the norm of φ_{lj}^{ps}, integrated up to r_c^l, to be equal to the norm of the corresponding two-component radial spinor. The pseudo-wave functions φ_{lj}^{ps} obey the pseudopotential Schrödinger equation with eigenvalues equal to the l- and j-dependent all-electron energies of the valence electrons,

$$\left(-\frac{\mathrm{d}^2}{\mathrm{d}r^2} + \frac{l(l+1)}{r^2} + V_{lj}^{\text{ps}}(r) - \epsilon_{lj}\right) \phi_{lj}^{\text{ps}}(r) = 0\,. \tag{21}$$

Note that the index n has been dropped here, since the orbital quantum numbers (lj) uniquely determine the pseudo-valence states [56, 57].

In the next step, the *screened* pseudopotential with components $V_{lj}^{\text{ps}}(r)$ can be obtained by inverting Eq. (21). It is this inversion that causes the pseudopotential to be lj-dependent despite the fact that the all-electron Kohn–Sham potential is lj-independent. The remaining task is to determine the ionic pseudopotential V^{ion}, i.e., the potential of a single valence electron in the field of the atomic core. This potential needs to be extracted from V_{lj}^{ps} through elimination of the electron-electron interaction between the pseudo-electrons. This so-called unscreening procedure is the major non-trivial step within the REXX scheme. In the neutral pseudo-atom, the pseudo-electrons move in an effective potential that may be written as a sum of the ionic pseudopotential V^{ion} and a screening potential $V_{\text{screen}}^{\text{ps}}$,

$$V_{lj}^{\text{ps}}(r) = V_{lj}^{\text{ion}}(r) + V_{\text{screen}}^{\text{ps}}([\rho^{\text{ps}}];\ r)\,, \tag{22}$$

$$V_{\text{screen}}^{\text{ps}}([\rho^{\text{ps}}];\ r) = v_H^{\text{ps}}([\rho^{\text{ps}}];\ r) + v_x^{\text{ps}}([\rho^{\text{ps}}];\ r) + v_c^{\text{ps}}([\rho^{\text{ps}}];\ r)\,. \tag{23}$$

The potential $V_{\text{screen}}^{\text{ps}}$ is a functional of the pseudo-electron density ρ^{ps} and contains the same density-functionals as the ones entering the all-electron calculation. In the LDA (or GGA) scheme, the Hartree potential v_H, the correlation potential v_c, as well as the exchange potential v_x are known explicit functions of the pseudo-electron density. In such a case, the unscreening of the atomic pseudopotentials can be performed straightforwardly by subtracting $V_{\text{screen}}^{\text{ps}}$ from V_{lj}^{ps} [55]. Similarly, the ionic pseudopotentials in the Hartree–Fock method [61–63] can be obtained simply by subtracting from V^{ps} the Coulomb and non-local exchange contribution due to the valence electrons. This contribution is an explicitly known functional of the pseudo-orbitals and has the same form as its all-electron correspondent because the Hartree–Fock Coulomb and exchange potential consists of additive contributions of all occupied orbitals. Similar arguments apply to other pseudopotential methods where the explicit dependence of the screening potential on the orbitals is known, such as in the self-interaction corrected LDA (SIC-LDA) [64]. In the REXX formalism, on the other hand, these standard methods of unscreening are not applicable, since neither the explicit dependence of v_x on the density nor on the orbitals is known. The solution consists in a application of the atomic OEP method to the pseu-

© 2004 WILEY-VCH Verlag GmbH & Co. KGaA, Weinheim

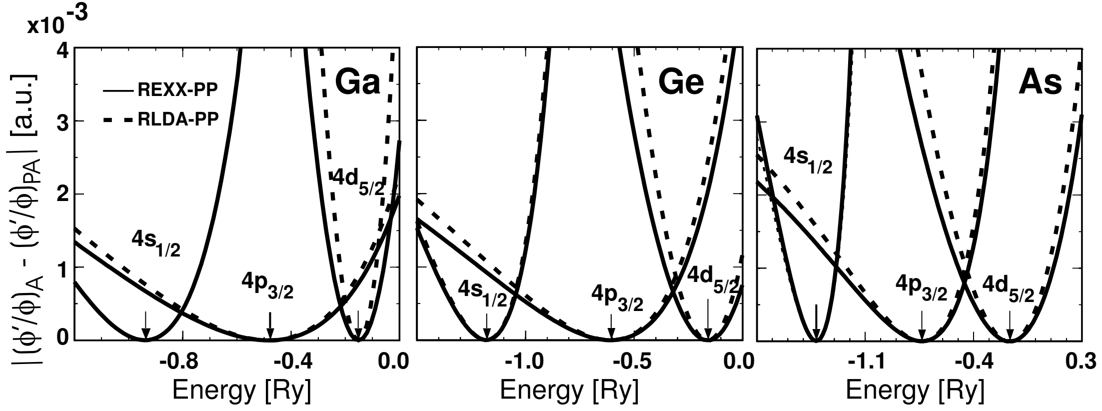

Fig. 3 Deviations between pseudoatomic (PA) and all-electron radial logarithmic derivatives (A) in atomic units, as calculated in the REXX and RLDA methods for the atoms Ga, Ge, and As. The arrows mark the energies in Rydbergs of the all-electron REXX orbital states. For better comparison, the RLDA curves for each orbital lj have been shifted horizontally in such a way that they coincide with the REXX curves at the marked energies. The same pseudopotential cutoff radius r_c (equal to 2.2, 1.9, and 2.2 for Ga, Ge, and As, respectively) has been used for all angular momentum components. The radial logarithmic derivatives are computed at $r = 2.4$ atomic units.

doatom. In other words, one solves the REXX equations for the pseudoatom in the form of the OEP integral equation and obtains v_x^{ps} [56, 57]. Since the density dependence of the Hartree potential is known, the ionic pseudopotential V_{lj}^{ion} can then be calculated from Eq. (22).

Since solid state calculations are often performed scalar-relativistically, it is useful to define the spin-averaged pseudopotential [17],

$$\overline{V}_l^{\text{ion}}(r) = \frac{l+1}{2l+1}\, V_{l,l+\frac{1}{2}}^{\text{ion}}(r) + \frac{l}{2l+1}\, V_{l,l-\frac{1}{2}}^{\text{ion}}(r) \; . \tag{24}$$

The difference between the radial logarithmic derivatives of the all-electron wave functions and pseudo-wave functions is a widely used measure for the transferability of a pseudopotential. Figure 3 depicts these differences for several atoms, as calculated within the REXX and RLDA, respectively. These deviations are seen to be systematically smaller in the REXX, indicating superior transferability.

As already pointed out, the EXX-Kohn–Sham potential possesses the correct asymptotic limit and consequently yields bound unoccupied orbitals in atoms, in contrast to LDA. Thus, all angular momentum components of the EXX pseudopotential can be treated on an equal footing, irrespective of their occupancy in the neutral atom. We have been able to demonstrate that the ionic REXX pseudopotentials only weakly dependent on the valence configuration and therefore show a better transferability than their LDA counterparts.

2.2.3 Results: Cohesive properties

The EXX scheme has been applied to the cohesive and electronic properties for quite a number of semiconductors [31]. As already explained, this method calculates the exchange energy exactly but does not deal with the correlation energy. For realistic predictions, however, correlations need to be included in a total energy calculation. Therefore, all calculations have been caried out either with no correlation potential (denoted by EXX(X)), with the standard LDA correlation potential [64] (denoted by EXX with no further addition), or with the GGA correlation functional [5] (denoted by EXX(GGA)). Standard LDA calculations with LDA exchange and correlation functionals are denoted by LDA. The pseudopotentials employed in the solid state calculations are consistent in the sense that they are constructed with the same Hamiltonian in the atom as is invoked in the solid.

© 2004 WILEY-VCH Verlag GmbH & Co. KGaA, Weinheim

Table 3 Theoretical LDA and EXX lattice constants (in Å) and bulk moduli (in Mbar) of Si, Ge, and GaAs, compared with experimental data (taken from Ref. [21] except where noted otherwise).

	LDA		EXX		expt.	
	a_0	B_0	a_0	B_0	a_0	B_0
Si	5.39	0.96	5.42	1.15	5.43	0.99
GaAs	5.61	0.74	5.70	0.85	5.65	0.77
GaN	4.49	1.93	4.47	2.39	4.50$^{(*)}$	

$^{(*)}$ – Reference [67]

The calculated EXX equilibrium lattice constants and bulk moduli are summarized in Table 3 and compared to LDA results as well as to experiment. The LDA values include nonlinear core corrections according to Ref. [65]. Generally, the lattice constants predicted by the EXX method are close to the LDA results, in spite of the fact that the EXX calculations do not include a nonlinear core correction [65]. The EXX method is seen to overestimate experimental bulk moduli by about 20%. This originates not from the core, but from the valence electrons since LDA calculations with EXX pseudopotentials tend to underestimate the experimental bulk moduli by 5–10%. It has been noticed before [66] that valence electron correlation effects tend to reduce Hartree–Fock bulk moduli by typically 20%. Thus, a treatment of correlations beyond LDA might be needed for obtaining more accurate bulk moduli in an exact exchange calculation.

Figure 4 compares the calculated EXX and EXX(GGA) cohesive energies with LDA and Hartree–Fock results and with experimental data [31]. Whereas the LDA results exhibit the well-known *overbinding* effect and overestimate the experimental data by 0.6–2.1 eV/atom, the EXX(GGA) cohesive energies are seen to agree excellently with experiment. To assess the origin of this good agreement, we have computed cohesive energies with related methods for comparison. We find that EXX(X), i.e. EXX without correlations, leads to cohesive energies that are virtually identical to Hartree–Fock values (cf. Fig. 4). Once one adds either LDA correlations or GGA correlations, the cohesive energies systematically increase and become closer to the experimental values. With LDA correlations, cohesive energies are still underestimated by 0.5–0.8 eV/atom, whereas GGA correlations produce those excellent EXX(GGA) results shown in Fig. 4. Similar findings have been reported by adding a GGA correlation functional to the Fock operator [68].

2.2.4 Results: EXX band structures

Figure 5 compares the calculated fundamental LDA and EXX band gaps for eight semiconductors with experimental data [31]. As is evident from these results, the EXX formalism leads to band gaps

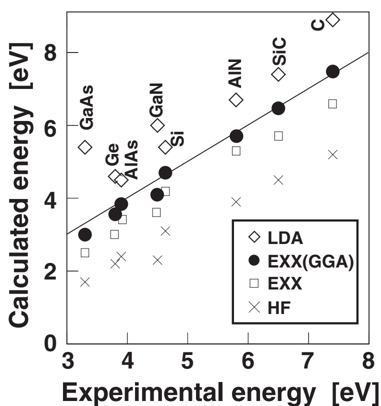

Fig. 4 Comparison of self-consistently calculated LDA, EXX, EXX(GGA), and Hartree–Fock cohesive energies (given in eV/atom) of various semiconductors with experimental data. The latter are taken from Refs. [21,69,70]. The solid line corresponds to perfect agreement between theory and experiment and is only drawn to guide the eye.

© 2004 WILEY-VCH Verlag GmbH & Co. KGaA, Weinheim

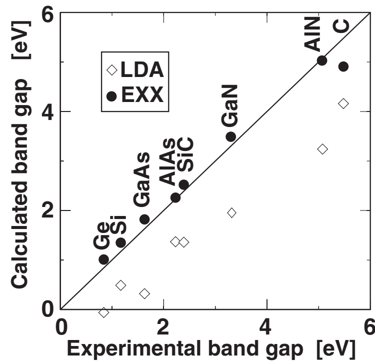

Fig. 5 Comparison of self-consistently calculated LDA and EXX band gaps (in eV) of various semiconductors with experimental data from References [21, 72–74].

that are in excellent agreement with experiment, the deviation being less than 0.1–0.3 eV. By contrast, the corresponding LDA values are too small by 1–1.5 eV. Noticeably, EXX gaps are much smaller than the corresponding Hartree–Fock values which are known to dramatically overestimate semiconductor band gaps. For example, we have computed the minimal Hartree–Fock energy gaps of Si, Ge, and GaAs to be 7.4, 6.4, and 7.7 eV, respectively, which is in accord with previously calculated results [71].

Correlations seem to have a weak influence on the energy gaps, as far as one can judge from the available correlation functionals [31]. Within an exchange-only EXX(X) calculation, one finds the energy gaps to decrease by typically less than 0.1 eV relative to the EXX results. For example, the minimal gaps within EXX(X) are 1.23, 0.94, and 1.78 eV for Si, Ge, and GaAs, respectively. By using GGA rather than LDA correlations in the solid state calculation, the energy gaps decrease slightly by typically 0.2 eV and amount to 0.97, 0.72, and 1.55 eV for Si, Ge, and GaAs, respectively.

The physical origin of the excellent agreement between EXX energy gaps and experiment lies in the absence of self-interaction and the locality of the exact exchange potential. Since the occupied valence states do not feel a self-repulsion in EXX, they become more localized and are energetically lowered relative to LDA. Hartree–Fock is only self-interaction free for the occupied but not for the unoccupied states. The nonlocality of the Fock exchange potential causes the unoccupied states to effectively see a different potential (N electrons) than the valence states (N-1 electrons) which gives rise to the huge energy gap in Hartree–Fock. By contrast, the EXX exchange potential is local and state-independent, and therefore the *same* for occupied as well as for unoccupied states.

The EXX approach not only shifts all band gaps upwards in energy, but additionally yields the correct ordering of the conduction band minima for all studied semiconductors. Thus, it faithfully reproduces the known $\boldsymbol{k}$-dependence of the band structure across the whole Brillouin zone. For Si and Ge, the dispersion relations are depicted in Fig. 6. In the case of Ge, the differences between LDA

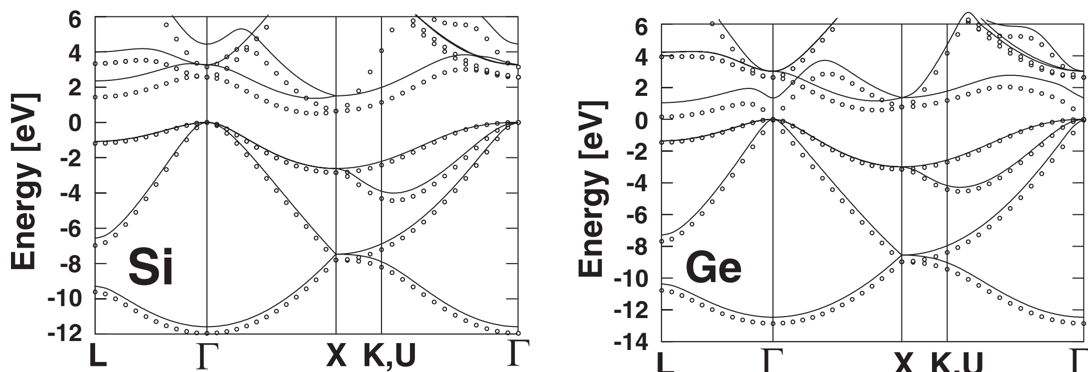

Fig. 6 Band structures for Si and Ge, as calculated within the LDA (open circles) and EXX (solid lines) methods, respectively.

© 2004 WILEY-VCH Verlag GmbH & Co. KGaA, Weinheim

and EXX gaps are particularly strongly $\boldsymbol{k}$-dependent. Whereas LDA incorrectly predicts a direct and negative energy gap at Γ, EXX correctly yields the conduction band minimum at L. The indirect nature of the energy gap of Ge originates predominantly in the Ge core. Indeed, by performing an LDA calculation for Ge bulk but employing EXX pseudopotentials, one already finds an indirect band gap at L that is lower than the direct one at Γ by 0.18 eV (the experimental value is 0.16 eV). Indeed, the importance of the core for reproducing the indirect band gap in Ge has been pointed out before [75].

These results lead to the question whether good band gaps may be obtained already by carrying out standard LDA calculations for the valence electrons and by employing pseudopotentials that are constructed with the EXX scheme. Indeed, such calculation yield generally larger band gaps in Γ and L and smaller in X points in comparison to pure LDA calculations. Especially the direct band gaps at Γ of GaAs and Ge are increased significantly relative to a strict LDA calculation, giving 0.86 (0.32) eV and 0.42 (−0.09) eV for GaAs, and Ge, respectively.

It has been also found that EXX calculations predict generally smaller band widths than LDA, irrespective of the type of pseudopotential used. This may be explained by the enhanced electron localization induced by the absence of self-repulsion in EXX. The only exceptions are the small core compounds C and AlN. This indicates that EXX slightly overestimates the localization of valence states since EXX band widths are generally a few percent smaller than the experimental values.

2.2.5 Results: EXX effective masses

Since the Kohn−Sham potential in the EXX approach is local, all momentum states see the same potential. This greatly simplifies band structure calculations relative to Hartree−Fock type or GW type methods [71, 76]. Therefore, EXX allows one to compute effective band masses as easily as LDA does. It is well known that LDA effective masses agree rather poorly with experimental data in some materials where the LDA predicted energy gap is much too small, such as GaAs where the LDA effective conduction band mass ($0.03m_0$) is by more than factor two smaller than the experimental one ($0.067m_0$) [77, 78]. The EXX method overcorrects the LDA error yielding an effective conduction band mass of $0.10m_0$ for GaAs [31]. Generally, EXX electron masses are found to be almost equal to or larger than the corresponding LDA masses and show systematically better agreement with experiment in cases were LDA fails markedly. This is in qualitative accord with standard $\boldsymbol{k}\cdot\boldsymbol{p}$ theory which predicts band masses to change roughly in proportion to energy gaps.

The Luttinger parameters [79] L, M, and N that characterize the warped structure of the three topmost valence bands near Γ point have been also investigated [31]. These parameters were determined numerically by fitting the three-band $\boldsymbol{k}\cdot\boldsymbol{p}$ band structure [79] to the LDA and EXX bands. In units of $\hbar^2/2m$, the triplet (−L, −M, −N) for GaAs is given by (56.56, 4.01, 57.71) within LDA and by (11.20, 3.48, 11.97) within EXX. In this case, EXX agrees substantially better with the experimental values [21] of (15.49, 3.94, 16.09) than LDA does. In some other materials, however, EXX tends to predict hole masses that are slightly too heavy which is consistent with the trends in the valence band widths. In Si, for example, we find (−L, −M, −N) to be given by (7.15, 4.75, 9.17), (5.64, 3.89, 6.86), and (6.64, 4.60, 8.68), within LDA, EXX, and experiment, respectively.

2.2.6 Dielectric functions

In this section we will show that the EXX approach not only yields excellent band gaps but also accurately predicts optical properties such as dielectric functions and reflectivities [31]. Figure 7 depicts a representative example, the imaginary part of the dielectric function of GaAs namely, which is given by

$$\varepsilon_2(\omega) = \frac{4\pi^2 e^2 \hbar^2}{3m^2 \Omega \omega^2} \sum_{vc\boldsymbol{k}} |\langle v\boldsymbol{k}|\, \boldsymbol{p}\, |c\boldsymbol{k}\rangle|^2 \; \delta(\hbar\omega - \varepsilon_{c\boldsymbol{k}} - \varepsilon_{v\boldsymbol{k}}) \,, \tag{25}$$

© 2004 WILEY-VCH Verlag GmbH & Co. KGaA, Weinheim

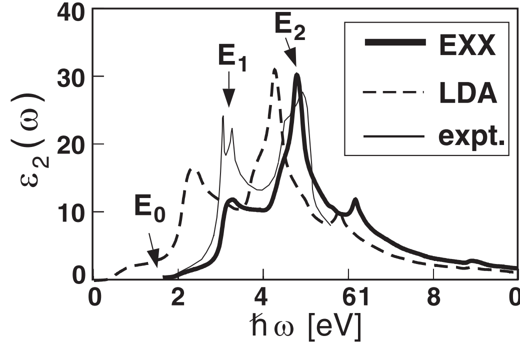

Fig. 7 Comparison of the calculated EXX and LDA imaginary part of the GaAs dielectric function as a function of energy (in eV) with experimental data from Reference [84]. Note that the present calculations do not include spin-orbit-splitting effects that lead to the splitting in the experimental E_1 peak.

where $\boldsymbol{p}$ is the momentum operator. The exchange-correlation, local field and nonlocal pseudopotential effects have been neglected in this expression, since they are known to have only a minor effect on the peak positions [80, 81]. For the $\boldsymbol{k}$ summation in Eq. (25), 328 $\boldsymbol{k}$ points in the irreducible wedge of the Brillouin zone were taken into account. It is apparent from Fig. 7 that the position of the EXX calculated absorption edge E_0 as well as of the two prominent peaks labeled E_1 and E_2 are much closer to the measured data than LDA. As is well known, a $\boldsymbol{k}$-independent scissors operator correction to the LDA band structure cannot achieve such an improvement [82]. In accord with other calculations [80, 81, 83], the height of the E_1 peak still does not fit the experimental one very well which may be caused by the neglect of excitonic, many-body, and surface effects.

In passing we note that quasiparticle corrections to EXX band gaps have been found to be small [85, 86] which provides another argument in favor of this method.

3 Relativistic electronic structure of semiconductors

While there is an ever increasing number of LDA-based ab-initio codes that are made available to the physics community (e.g. the Fritz haber code FHI98md), only very few codes include relativistic, particularly spin-orbit effects, nonperturbatively. Since spin lifetimes in semiconductors have become a central issue for quantum information, however, LDA calculations of spin-orbit related effects in semiconductors have become very relevant.

In this section, we present an implementation of the relativistic LDA method including the construction of relativistic pseudopotentials for semiconductor structures, assess their accuracy and provide some illustrative applications. This is new material that has not been published so far. We note that the spin-orbit interaction in semiconductors arises from the p- and d-electrons in the core and thus enters the electronic Hamiltonian only in the ionic pseudopotential explicitly since the gradients of the potential generated by the valence electrons are much weaker than the gradients of the ionic potential.

3.1 Relativistic ionic separable pseudopotential

The ionic pseudopotential for an atom can be written in terms of the pseudopotential components $V_{lj}^{\text{ion}}(r)$ introduced in Sect. 2.2.2 as follows

$$V_{\text{ion}}^{\text{ps}}(\boldsymbol{r}) = \sum_{ljm} |ljm\rangle\, V_{lj}^{\text{ion}}(r)\, \langle ljm| \,, \tag{26}$$

where $|ljm\rangle \equiv Y_{ljm}(\boldsymbol{r})$ are spherical spinors, and $j = l \pm 1/2$. The atomic pseudopotential can be split into the scalar relativistic spin-averaged pseudopotential and the spin-orbit pseudopotential [17]

$$V_{\text{ion}}^{\text{ps}}(\boldsymbol{r}) = \sum_{lm} |ljm\rangle\, [\overline{V}_{l}^{\text{ion}}(r) + \overline{V}_{l,\text{so}}^{\text{ion}}(r)\, \boldsymbol{L}\cdot\boldsymbol{S}]\, \langle lm| \,, \tag{27}$$

© 2004 WILEY-VCH Verlag GmbH & Co. KGaA, Weinheim

where $\overline{V}_l^{\text{ion}}(r)$ and $\overline{V}_{l,\text{so}}^{\text{ion}}(r)$ are given by

$$\overline{V}_l^{\text{ion}}(r) = \frac{l+1}{2l+1}\, V_{l,l+1/2}^{\text{ion}}(r) + \frac{l}{2l+1}\, V_{l,l-1/2}^{\text{ion}}(r)\,, \tag{28}$$

$$\overline{V}_{l,so}^{\text{ion}}(r) = \frac{2}{2l+1}\, [V_{l,l+1/2}^{\text{ion}}(r) - V_{l,l-1/2}^{\text{ion}}(r)]\,. \tag{29}$$

The first term in Eq. (27) contains all scalar parts of the relativistic pseudopotential, mass velocity and Darwin contributions, and is included into any available pseudopotential scheme, whereas the second term is the spin-orbit interaction and has only rarely been taken into account. The vector part of the nonlocal pseudopotential can be treated exactly or as a perturbation [18, 87]. In both ways, the spin-orbit splitting of the valence bands near Γ point in bulk Ge, GaAs, and InSb has been calculated [18, 87]. In superlattices or systems with many atoms per unit cell, however, the computational effort of its calculation rises sharply, since the vector part of the nonlocal pseudopotential cannot be cast into a separable form [88] that greatly facilitates LDA total energy calculations. Fortunately, this problem is only associated with the averaging procedure in Eq. (28) and a separable form of the entire relativistic nonlocal pseudopotential can be constructed indeed [89, 90]. This is the approach that we have pursued. The entire relativistic nonlocal separable pseudopotential can be written as

$$\overline{V}_{\text{ion}}^{\text{sep}}(\boldsymbol{r}) = V_{\text{loc}} + \sum_{ljm} \frac{|\delta V_{lj}\, R_{lj} Y_{ljm}\rangle\, \langle \delta V_{lj}\, R_{lj} Y_{ljm}|}{\langle R_{lj}|\, \delta V_{lj}\, |R_{lj}\rangle}\,, \tag{30}$$

where $\delta V_{lj} = V_{lj}^{\text{ion}} - V_{\text{loc}}$, and V_{loc} simply represents one (arbitrarily) chosen lj component of the pseudopotential, R_{lj} is the radial part of the pseudofunction that fulfils Eq. (21), and Y_{ljm} is the spherical spinor. The latter function can be decomposed into spherical harmonics Y_m^l and spin functions χ_+ and χ_-,

$$Y_{l,j=l\pm 1/2,m_j} = \pm\sqrt{\frac{l \pm m_j + \frac{1}{2}}{2l+1}}\, Y_{m_j-1/2}^l \chi_+ + \sqrt{\frac{l \mp m_j + \frac{1}{2}}{2l+1}}\, Y_{m_j+1/2}^l \chi_-\,. \tag{31}$$

These expressions are then inserted into Eq. (30). The plane wave basis $|\boldsymbol{G}\rangle$ ($\boldsymbol{G}$ labels the reciprocal vectors) is now doubled and contains states corresponding to both spin directions $|\boldsymbol{G},+\rangle = |\boldsymbol{G}\rangle\chi_+$, and $|\boldsymbol{G},-\rangle = |\boldsymbol{G}\rangle\chi_-$. The calculation of the matrix elements of the relativistic nonlocal separable pseudopotential in this doubled basis is rather straightforward. The doubled Kohn–Sham Hamiltonian matrix is diagonalized using standard iterative techniques. A similar approach based on separable pseudopotentials has already been proposed by Hemstreet et al. [19]. However, their approach neglected terms of higher than first order in $\overline{V}_{l,so}^{\text{ion}}$ and treated spin-orbit terms in first order perturbation theory. Therefore, the spin-orbit terms do not contribute to the ground state energy in the scheme of Ref. [19]. By contrast, the ground state total energy contains all relativistic effects in the present scheme. This procedure for incorporating the spin-orbit interaction into an ab-initio pseudopotential calculation can be implemented in any version of density functional theory, such as LDA, GGA, SX-LDA, or EXX.

3.2 Results: Split-off valence bands in zinc-blende and wurtzite semiconductors

To illustrate the accuracy of relativistic pseudopotential LDA calculations, we calculated the top valence band spin-splitting $\Delta_0 = \epsilon(\Gamma_{8v}) - \epsilon(\Gamma_{7v})$ in the Γ-point for several III–V zinc-blende and wurtzite semiconductors. The results are depicted in Fig. 8 and compared to experiment. The agreement with experimental data is excellent. The results show that the magnitude of Δ_0 is largely determined by the anion which is consistent with the anion *p*-type character of the valence band in the compounds considered. Thus, Δ_0 follows the atomic trends of the spin-orbit splitting.

In the wurtzite structure, the top of the valence band at the Γ point consists of a doubly degenerate Γ_9 and two doubly degenerate Γ_7 states. At zero strain, the doubly degenerate energies of the valence

© 2004 WILEY-VCH Verlag GmbH & Co. KGaA, Weinheim

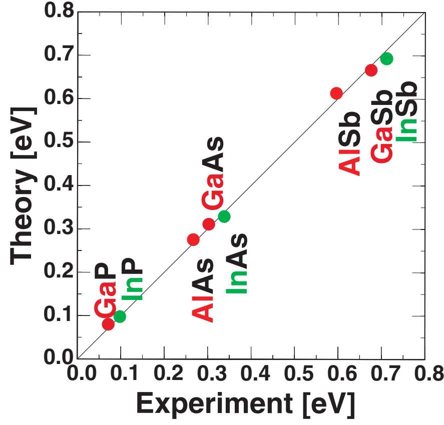

Fig. 8 Comparison of the calculated and experimental spin splitting of the valence band in several semiconductors.

band maximum are conventionally written as [91]

$$E(\Gamma_9) = \frac{1}{3}\Delta_1 + \Delta_2 \,, \tag{32}$$

$$E(\Gamma_{7+}) = -\frac{1}{2}\left(\frac{\Delta_1}{3} + \Delta_2\right) + \sqrt{\left(\frac{\Delta_1 - \Delta_2}{2}\right)^2 + 2\Delta_3^2} \,, \tag{33}$$

$$E(\Gamma_{7-}) = -\frac{1}{2}\left(\frac{\Delta_1}{3} + \Delta_2\right) - \sqrt{\left(\frac{\Delta_1 - \Delta_2}{2}\right)^2 + 2\Delta_3^2} \,, \tag{34}$$

where the center of gravity of these three bands has been set to zero. The constants Δ_2 and Δ_3 are spin-orbit Hamiltonian matrix elements, whereas Δ_1 is conventionally termed the crystal-field splitting. This constant can be independently determined by performing nonrelativistic calculations [92, 93]. When this constant obey the condition $\Delta_1 > 0$ these band states are ordered such that $\Gamma_{7-} < \Gamma_{7+} < \Gamma_9$ [92, 93]. This is fulfilled in GaN and InN. The opposite case of $\Delta_1 < 0$ is realized in AlN. In that case, the states form the sequence $\Gamma_{7-} < \Gamma_9 < \Gamma_{7+}$ [92, 93]. Once the constant Δ_1 has been determined, one can extract the spin-orbit splitting constants Δ_2 and Δ_3 from relativistic band structure calculations [92, 93]. This procedure yields (Δ_1, Δ_2, Δ_3) equal to (–219, 6.6, 6.7) meV and (24, 5.4, 6.8) meV for AlN and GaN, respectively.

The exciton energies corresponding to these split valence edge states have been recently measured in strained GaN films [94, 95] and in relatively thick AlN layers [96]. For AlN, the calculated and measured (in parenthesis) energy differences agree perfectly with one another and are given by $E(\Gamma_{7+}) - E(\Gamma_9)$ = 213 (210) meV, and $E(\Gamma_9) - E(\Gamma_{7-})$ = 14 (20) meV. Our relativistic LDA calculations included strain effects since the exciton energies in GaN have been measured in biaxially strained films. The calculated positions of the three valence levels $E(\Gamma_9)$, $E(\Gamma_{7+})$, and $E(\Gamma_{7-})$ are plotted in Fig. 9 as a function of biaxial strain and compared to the experimental data. We note that the spin-orbit splitting constants Δ_2 and Δ_3 are nearly independent of strain.

3.3 Results: Spin-orbit splitting at a general wave vector

In the previous chapter, we discussed the splitting of the top of the valence band at Γ caused by the spin-orbit interaction. However, all states at Γ remain at least doubly degenerate (Kramers degeneracy). In a system that lacks invesion symmetry, this two-fold spin degeneracy holds at Γ and along certain symmetry lines but is lifted at a general Bloch electron wave vector. The spin splitting near the band extrema manifests itself in a range of physical phenomena such as polarized luminescence or spin-relaxation. Since it is extremely difficult to measure the magnitude of the spin-splitting away

© 2004 WILEY-VCH Verlag GmbH & Co. KGaA, Weinheim

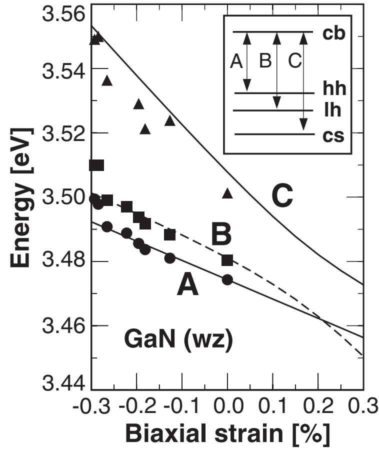

Fig. 9 Comparison of experimental free exciton energies of strained GaN from Ref. [95], and unstrained GaN [97] (full dots, squares, and triangles denote energies of A, B, and C exciton lines, respectively) with theoretical calculations (lines) [93]. The theoretically calculated energies were rigidly shifted by 1.209 eV. This energy shift includes the self-energy correction to the LDA gaps and the exciton binding energy.

from the high symmetry band extrema, reliable theoretical predictions of the spin-splitting are of great importance for a quantitative description and understanding of spin phenomena in semiconductors.

We consider here the spin-splitting in zinc-blende materials near the Γ point. In bulk zinc-blende binary compounds, the conduction and split-off valence bands, of Γ_6 and Γ_7 symmetry, respectively, exhibit a spin-splitting of order k^3 that is strongly anisotropic [98]. This spin-splitting is given by

$$\Delta E = 2\gamma\sqrt{\Omega_x^2 + \Omega_y^2 + \Omega_z^2}\,, \tag{35}$$

where $\Omega_x = k_x(k_y^2 - k_z^2)$, and $\Omega_y = k_y(k_z^2 - k_x^2)$, and $\Omega_z = k_z(k_x^2 - k_y^2)$ and γ is a constant. We have calculated the value of this so-called Dresselhaus constant with our LDA calculations, using the relativistic separable pseudopotential method detailed above. For conduction band of GaAs, we find a value of γ_c = 44.3 eV Å^3. For the split-off band, this constant is given by γ_{so} = 50.4 eV Å^3. Both of these values agree very well with predictions using semilocal (i.e. non-separable) pseudopotentials [18] that give γ_c and γ_{so} equal to 50 eV Å^3, and 45 eV Å^3, respectively. We note that LDA-LMTO calculations produce even larger values, γ_c = 82 eV Å^3 [100]. However, by empirically adjusting the LDA energy gap to the experimental value, this Dresselhaus constant gets reduced to about 15 eV Å^3 [99]. The experimental value of $\gamma_c = 25.5$ eV Å^3 [99] lies in between these values. Thus, spin-splitting of the first conduction band is strongly dependent on the energy gap.

In the manifolds of top valence bands that arise from the Γ_8 state, there are linear-k spin-splitting terms. The energies of the four top valence bands are given, for small values of k [101],

$$\epsilon = \pm C[k^2 \pm [3(k_x^2k_y^2 + k_y^2k_z^2 + k_x^2k_z^2)]^{\frac{1}{2}}]^{\frac{1}{2}}\,. \tag{36}$$

Our pseudopotential calculations yield C = 4.9 meV Å for bulk GaAs, which compares well with other pseudopotential [18] and LMTO [99] calculations, where values of C = 3.4 meV Å and C = 3.6 meV Å have been obtained, respectively. The linear-k terms originate in atomic d-states to the valence band states. If one constructs pseudopotentials without any d (and higher angular momentum) components, one does not obtain linear k spin-splittings. In contrast to the situation with the lowest conduction band, the magnitude of C depends only weakly on the energy gap. In order to assess this dependence, we calculated the band structure of GaAs as a function of hydrostatic pressure. For pressures that change the energy gap by a factor of three, the constant C changes only by 20%, whereas the value of γ_c changes by 830%. The latter result agrees with earlier perturbative calculations [100].

4 Electronic structure methods for mesoscopic systems

Once the number of atoms per unit cell (or supercell) exceeds a few hundred, microsocopic methods that take into account the detailed atomistic structure become not only unfeasable altogether but also impractical as the observables of interest are slowly varying over atomic distances. In spite of many

© 2004 WILEY-VCH Verlag GmbH & Co. KGaA, Weinheim

attempts to develop alternatives, there is still only one established and well-studied electronic structure method that is suitable for systems of mesoscopic length scales. This is the enveloppe function approach that is based on the $\boldsymbol{k}\cdot\boldsymbol{p}$-method [102–105].

In spite of its known limitations and shortcomings [106], this method has been amazingly successful in predicting semiconductor nanostructures. For heterostructures, there are two variants of this method that are most commonly employed, one that is based on the original Kohn–Luttinger approach [102, 103] and another one that is based on the work by Burt and Foreman [104, 105], but the results differ only insignificantly [107].

Based on the enveloppe function approach, we have developed a realistic simulator of three-dimensional semiconductor nano-structures and optoelectronic nano-devices over the last few years that we termed nextnano^3 [108–110]. Such a program package must meet two requirements. Firstly, it should model the electronic structure of any combination of quantum wells, wires, and dots accurately on a length scale from nm to μm. Secondly, a device simulator should self-consistently account for the charge redistribution under applied voltage and for the resulting current [111]. Several models of this kind have been developed in the last few years that can deal with fully three-dimensional device geometries, and invoke one-band [112], or several-band $\boldsymbol{k}\cdot\boldsymbol{p}$-models [113–116]. Here, we review the basic methods and some results obtained with nextnano^3 [108–110] that meet both requirements mentioned above. As concrete examples, we discuss a study of self-assembled GaAs/InAs single-quantum dot photodiodes [117] and the relation between alloy profiles and exciton Stark shifts in such quantum dots.

4.1 Three-dimensional nanodevice simulator nextnano^3

The simulator [108–110] solves the 8-band-$\boldsymbol{k}\cdot\boldsymbol{p}$-Schrödinger-Poisson equation for arbitrarily shaped 3-D heterostructure device geometries, and for any (III–V and Si/Ge) combination of materials and alloys. It includes band offsets of the minimal and higher band edges, absolute deformation potentials [118], local density exchange and correlations (i.e. the Kohn–Sham equations), total elastic strain energy [116, 120], long-range Hartree potential induced by charged impurity distributions, voltage induced charge redistributions, piezo- and pyroelectric charges, as well as surface charges, in a self-consistent manner. The charge density is calculated for a given applied voltage by assuming the carriers to be in a local equilibrium characterized by energy-band dependent local quasi-Fermi levels $E_{\mathrm{F}c}(\boldsymbol{x})$ for charge carriers of type c (i.e. in the simplest case, one for holes and one for electrons),

$$n_c(\boldsymbol{x}) = \sum_i |\Psi_{ic}(\boldsymbol{x})|^2 f\left(\frac{E_{\mathrm{F}c}(\boldsymbol{x}) - E_{ic}}{k_{\mathrm{B}}T}\right). \tag{37}$$

These local quasi-Fermi levels are determined by global current conservation $\nabla\cdot\boldsymbol{j}_c = 0$, where the current is assumed to be proportional to the density and to the gradient of the quasi-Fermi level (associated with each band) exactly as in the semiclassical limit (see, e.g. [121]),

$$j_c(\boldsymbol{x}) = \mu_c n_c(\boldsymbol{x})\ \nabla E_{\mathrm{F}c}(\boldsymbol{x}). \tag{38}$$

The carrier wave functions Ψ_{ic} and energies E_{ic} are calculated by solving the multi-band Schrödinger-Poisson equation. The open system is mimicked by using mixed Dirichlet and von Neumann boundary conditions [119, 122, 123] at Ohmic contacts. The charge density at these contacts is assumed to be equal to the bulk equilibrium density. Thus, the quasi-Fermi levels and the potential in the contact region are fixed according to the applied voltage. Our method leads to globally orthogonal eigenstates including valence (split-off, light and heavy hole) and conduction band states. Further, it automatically includes tunneling, and yields optical transition energies and as well as optical matrix elements and can take into account magnetic fields.

4.1.1 Computational scheme

The computational methods employed solve the Kohn–Sham-Schrödinger, Poisson and current continuity equations iteratively using conjugate gradient, inverse-iteration, Jacobi-Davidson [124] and predictor-corrector methods [125] in an inhomogeneous finite difference framework.

© 2004 WILEY-VCH Verlag GmbH & Co. KGaA, Weinheim

For a given nano-structure, the computations start by globally minimizing the total elastic energy [126] using a conjugate gradient method. This determines the piezo-induced charge distributions, the deformation potentials and band offsets. Subsequently, the 8-band-Schrödinger, Poisson, and current continuity equations are solved iteratively. All equations are discretized according to the finite difference method invoking the box integration scheme [112, 124]. The irregular rectilinear mesh is kept fixed during the calculations. As a preparatory step, the built-in potential is calculated for zero applied bias by solving the Schrödinger and Poisson equation self-consistently employing a predictor-corrector approach [125] and setting to zero the electric field at the Ohmic contacts. For applied bias, the Fermi level and the potential at the contacts are then shifted according to the applied potential which fixes the boundary conditions. The main iteration scheme itself consists of two parts. In the first part, the wave functions and potential are kept fixed and the quasi-Fermi levels are calculated self-consistently from the current continuity equations, employing a conjugate gradient method and a simple relaxation scheme. In the second part, the quasi-Fermi levels are kept constant, and the density and the potential are calculated self-consistently from the Schrödinger and Poisson equation. The discrete 8-band-Schrödinger equation represents a huge sparse matrix (typically of dimension 10^6 for 3D-structures) and is diagonalized using the Jacobi–Davidson method [124] that yields the required inner eigenvalues and eigenfunctions close to the energy gap. We very slightly shift the spin-up and spin-down diagonal Hamiltonian matrix elements with respect to each other in order to avoid degeneracies and guarantee orthogonal eigenstates automatically. To reduce the number of necessary diagonalizations, we employ an efficient predictor-corrector approach [125] to calculate the potential from the nonlinear Poisson equation. In this approach, the wave functions are kept fixed within one iteration and the density is calculated perturbatively from the wave functions of the previous iteration [125]. The nonlinear Poisson equation is solved using a modified Newton method, employing a conjugate gradient method and line minimizations. The code is written in Fortran 90 and consists of some 200000 lines by now.

4.1.2 Application: Piezoelectric fields and electron-hole localization in quantum dots

As a first application, we discuss a theoretical analysis of single-quantum-dot photodiodes consisting of self-assembled InGaAs quantum dots with a diameter of 30–40 nm and heights of 4–8 nm that are embedded in the intrinsic region of a Schottky diode [109]. Recent experiments [117, 127] have indicated inverted electron-hole alignments with the electron at the base and the hole at the top of the dot, in contrast to what earlier theoretical calculations [114, 115] had predicted. This study reveals that the elastic strain and accompanying piezoelectric fields strongly depend on the geometric shape and alloy composition of dots. We find, in agreement with [113], dots of pyramidal shape to possess large piezoelectric polarization charges in the corners that lead to a strong hole confinement near the dot edges (Fig. 10a). By contrast, lens-shaped dots of similar size have much weaker charges and are found to lead to electron and hole states near the center of the lens which significantly improves the exciton absorption (Fig. 10b).

4.1.3 Application: Vertical and lateral Stark shifts of excitons in quantum dots

In this section, we present systematic predictions of the bias dependence of the electronic structure of self-assembled quantum dots for a wide variety of dot shapes, alloy profiles and show that the combined effect of applied and (piezoelectric) internal electric fields yields detailed information about shape and composition profiles. We note that the computational efficiency of nextnano^3 has allowed us to study hundreds of configurations and biases systematically. We have obtained a detailed understanding of the excitonic properties in quantum dots as a function of lateral as well as vertical electric fields. We were able to show that these field dependent excitonic transition energies provide unambiguous information about the shape and alloy composition of the quantum dot in all 3 dimensions, including the vertical and lateral variations of the Indium concentration in the InGaAs quantum dot.

The excitonic energy has been calculated self-consistently within the Hartree approximation. Assuming a separable exciton wave function, the Coulomb interaction between electron and hole is

© 2004 WILEY-VCH Verlag GmbH & Co. KGaA, Weinheim

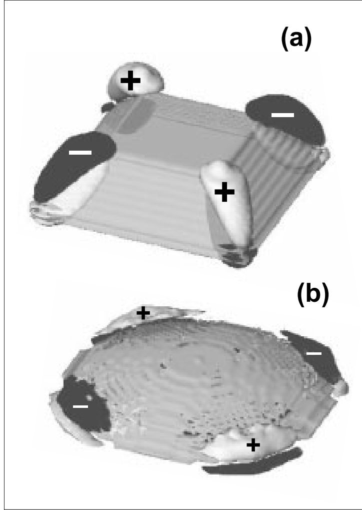

Fig. 10 Side view of calculated (a) pyramid-shaped and (b) lens-shaped InGaAs quantum dots. The height in the center is 8 nm for both dot shapes. The light and dark regions are isosurfaces of the positive and negative piezoelectric charge densities, respectively, with a magnitude of $5\times\ 10^{18}$ e/cm^3.

calculated by iteratively solving the Poisson and Schrödinger equation for each particle taking into account external and internal potentials including image charges due to the variation of the dielectric constant.

The simulated structure consists of a 20 nm thick GaAs substrate, a 1 nm wetting layer with an Indium content of 50% and the quantum dot with an In concentration that varies from 50% to 100%. The dot is capped by a GaAs layer. We have examined two classes of quantum dot shapes that have been discussed in the literature [113, 128, 129], lens-shaped and truncated pyramidal ("obelisk") dots namely. The height of the quantum dot has been systematically varied from 3 to 5 nm and the base width from 15 to 25 nm, respectively. These values lie within the range of experimentally estimated dot sizes. In addition, we considered two types of alloy profiles, a simple linear and an angular profile. In the latter case, the Indium concentration varies with the polar angle relative to the center axis of the dot. This profile is supported by STM measurements and by theoretical models [130] of the growth process and leads to an inverted pyramid of high Indium content inside the quantum dot. The most important feature of this alloy profile is the fact that it produces a vertical and a lateral variation of the Indium concentration which has been neglected so far.

The change of the single exciton transition energy in response to an applied bias, i.e. the quantum-confined Stark shift, is a widely studied effect in quantum dots [117, 128, 131–136]. So far, theoretical and experimental work focused solely on the effect of vertical electric fields applied along the quantum dot growth axis. However, fabrication of four terminal photodiode structures that incorporate a pair of implanted top contacts in a lateral split-gate geometry, in addition to a vertical MIS photodiode structure, would enable the simultaneous application of vertical and lateral electric fields. Devices incorporating such lateral capacitor concepts have already been realized in the II–VI system [134], enabling application of laterally orientated electric fields in the range ± 20 kV/cm. Our calculations show that the analysis of the response of the exciton wave function to simultaneously applied lateral and vertical electric fields provides a whole new inside into the structure and the composition of the quantum dot.

We have studied three different lateral field directions in the present calculations as shown in Fig. 11. Note that the strain and the resulting piezoelectric charges lead to an asymmetry which is reflected in the different Stark shifts for the various directions.

We have calculated the ground state exciton energy as a function of the vertical (F_v) and lateral (F_l) electric field and have fit the resulting Stark curves to a biquadratic form,

$$E(F_l, F_v) = E_0 + p_l F_l + p_v F_v + \chi_l F_l^2 + \chi_v F_v^2 + \chi_{lv} F_l F_v \ . \tag{39}$$

© 2004 WILEY-VCH Verlag GmbH & Co. KGaA, Weinheim

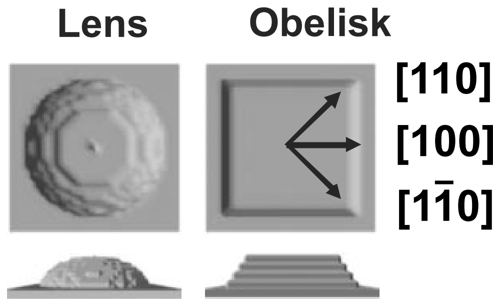

Fig. 11 Two types of quantum dot shapes considered in this work: lens and obelisk shapes. The height and base width of these dots are varied between 3 to 5 and 15 to 25 nm respectively. The directions of the lateral electric fields that are taken into account are indicated.

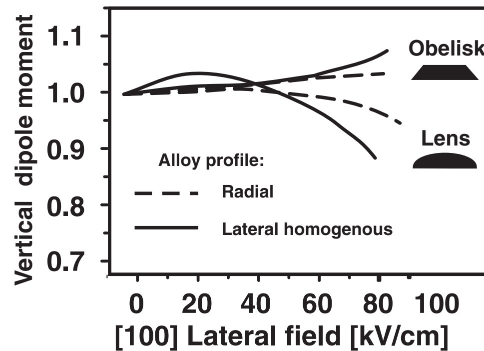

Fig. 12 Ratio of the vertical excitonic dipole moment relative to its zero field value for the 2 classes of quantum dot shapes and alloy profiles, respectively, as a function of the lateral field.

Here, E is the excitonic transition energy, E_0 the zero-field energy, p_v and p_l are the intrinsic (vertical and lateral) dipole moments along the field that reflect the zero-field separation of the electron and hole wave function and χ_v, χ_l are the (vertical and lateral) polarizabilities.

4.1.4 Vertical dipole moment as a function of the lateral electric field

Our calculations show that the change of the vertical dipole moment that follows from the response of the exciton to the vertical field for given lateral electric field depends very sensitively on the shape of the quantum dot. In fact, the vertical dipole moment increases with increasing lateral electric field for the obelisk shaped dots but decreases for the lens shaped QDs (see Fig. 12). This is true irrespective of the type of alloy profile even though the effect is less pronounced for the radial profile due to the stronger lateral confinement of the hole. The physical origin of the pronounced lateral field dependence of the dipole moment may be understood as follows. The hole wave function is always located near the tip of the QD and thus basically moves along the surface of the dot when a lateral field is applied. The electron wave function, on the other hand, is more extended and remains delocalized within the entire QD up to fairly high values of the lateral field. Since the top part of the obelisk QD is flat, the center of mass of the hole stays at a constant height and moves along the surface with increasing lateral field. This effect alone would lead to a constant dipole moment. However, the large strain at the edge of the obelisk deforms the confining potential in such a way that the hole gets partly localized outside the QD. This leads to an increase in the dipole moment. By contrast, a lens shaped QD possesses a curved surface that becomes thinner towards the edge so that the vertical distance between the centers of mass of hole and electron wave function necessarily decreases with increasing field. This explains qualitatively the results shown in Fig. 12. We note that fairly high lateral fields of more than 50 kV/cm are needed for observing a significant change in the dipole moment which may not be easy to realize experimentally.

4.1.5 Lateral polarizability for different alloy profiles

The polarizability of the exciton in a lateral electric field is another sensitive measure of the alloy profile of the quantum dot that depends particularly on the base width of the QD (see Fig. 13). In the case of the vertically linear alloy profile, one has a laterally homogeneous Indium concentration. Not surprisingly, this yields a very large polarizability for both types of QD shapes. The radial alloy profile, on the other hand, leads to an inverted pyramid of Indium content in the QD that in turn gives

© 2004 WILEY-VCH Verlag GmbH & Co. KGaA, Weinheim

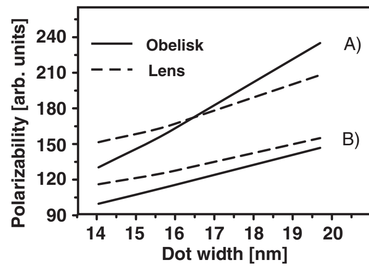

Fig. 13 Predicted lateral polarizability shown as a function of the base width of the quantum dot for different shapes and alloy profiles. The polarizability is much larger for dots (A) with a laterally homogenous alloy profile than for (B) dots with a radial profile since the latter provides a strong lateral confinement for the hole. For both alloy profiles, the results are shown for obelisk-shaped (full lines) as well as for lens-shaped quantum dots (dashed lines).

a strong lateral confinement of the hole. This effect reduces the polarizability drastically, typically by a factor of 2 compared to the linear alloy profile. Therefore, the alloy profile can be determined once the width of the quantum dot is known. The dots with a radial profile show a base width dependence of the polarizability that is very similar for both types of QD shapes. By contrast, QD with a laterally homogeneous profile possess a strong width dependence of the polarizability when they are obelisk-shaped but a weak one in the lens-shaped case. This is due to the fact that the curved surface of the lens QD enhances the lateral confinement which in turn limits the polarizability.

Acknowledgements We gratefully acknowledge financial support by the Deutsche Forschungsgemeinschaft and by the Office of Naval Research under Contract No. N00014-01-1-0242.

References

[1] G. Klimeck, F. Oyafuso, P. von Allmen, T. B. Boykin, and R. C. Bowen, Nanotech2003, February 23–27, 2003, San Francisco.
[2] L. W. Wang, A. Franceschetti, and A. Zunger, Phys. Rev. Lett. **78**, 2819 (1997).
[3] K. Ohno, K. Esfarjani, and Y. Kawazoe, Computational Materials Science, (Springer-Verlag, Berlin, 1999).
[4] W. Kohn and I. J. Sham, Phys. Rev. A **140**, 1133 (1965).
[5] J. P. Perdew, Phys. Rev. B **33**, 8822 (1986); ibid. **34**, 7406 (1986) (E).
[6] J. P. Perdew and Y. Wang, Phys. Rev. B **45**, 13244 (1992).
[7] A Primer in Density Functional Theory, Lecture Notes in Physics, editors C. Fiolhais, F. Nogueira, and M. Marques (Springer, Berlin, 2003).
[8] L. Hedin and S. Lundqist, in: Solid State Physics, Vol. 23, edited by F. Seitz, D. Turnbull and H. Ehrenreich (Academic Press, New York, 1969) p. 1.
[9] M. S. Hybertsen and S. G. Louie, Phys. Rev. B **23**, 4033 (1988).
[10] B. M. Bylander and L. Kleinman, Phys. Rev. B **41**, 7868 (1990).
[11] A. Seidl, A. Görling, P. Vogl, J. A. Majewski, and M. Levy, Phys. Rev. B **53**, 3764 (1996-I).
[12] V. Sahni, J. Gruenebaum, and J. P. Perdew, Phys. Rev. B **26**, 4371 (1982).
[13] C. B. Geller, W. Wolf, S. Picozzi, A. Continenza, R. Asahi, W. Mannstadt, A. Freeman, and E. Wimmer, Appl. Phys. Lett. **79**, 368 (2001).
[14] J. E. Robinson, F. Bassani, R. S. Knox, and J. R. Schrieffer, Phys. Rev. Lett. **9**, 215 (1962).
[15] J. Ihm, A. Zunger, and M. L. Cohen, J. Phys. C **12**, 4409 (1979).
[16] W. E. Pickett, Phys. Rep. **9**, 117 (1989).
[17] G. B. Bachelet, D. R. Hamann, and M. Schlüter, Phys. Rev. B **26**, 4199 (1982).
[18] M. P. Surh, Ming-Fu Li, and S. G. Louie, Phys. Rev. B **43**, 4286 (1991).
[19] L. A. Hemstreet, C. Y. Fong, and J. S. Nelson, Phys. Rev. B **47**, 4238 (1993).
[20] S. Massidda, A. Continenza, A. J. Freeman, T. M. de Pascale, F. Meloni, and M. Serra, Phys. Rev. B **41**, 12079 (1990).
[21] Numerical Data and Functional Relationships in Science and Technology, edited by K.-H. Hellwege, Landolt-Börnstein, New Series, Group III; Vol. 17 and Vol. 22 edited by O. Madelung, M. Schulz, and H. Weiss (Springer, Berlin, 1982), Vol. 23a edited by A. Goldman and E.-E. Koch (Springer, Berlin, 1989).
[22] J. E. Ortega and F. J. Himpsel, Phys. Rev. B **47**, 2130 (1993).
[23] R. Hulthen and N. G. Nilsson, Solid State Commun. **18**, 1341 (1976).
[24] D. Straub, L. Ley, and F. J. Himpsel, Phys. Rev. Lett. **54**, 142 (1985).
[25] D. E. Eastman, W. D. Grobman, J. L. Freeouf, and M. Erbudak, Phys. Rev. B **9**, 600 (1974).

© 2004 WILEY-VCH Verlag GmbH & Co. KGaA, Weinheim

[26] F. D. Murnaghan, Proc. Natl. Acad. Sci. USA **30**, 244 (1944).
[27] J. D. Wiley, in Semiconductors and Semimetals, edited by R. K. Willardson and A. C. Beer, Vol. 10 (Academic, New York, 1975), p. 134.
[28] V. Fiorentini, Phys. Rev. B **46**, 2086 (1992).
[29] R. Asahi, W. Mannstadt, and A. J. Freeman, Phys. Rev. B **59**, 7486 (1999).
[30] R. Asahi, W. Mannstadt, and A. J. Freeman, Phys. Rev. B **62**, 2552 (2000).
[31] M. Städele, M. Moukara, J. A. Majewski, P. Vogl, and A. Görling, Phys. Rev. B **59**, 10031 (1999).
[32] J. D. Talman and W. F. Shadwick, Phys. Rev. A **14**, 36 (1976).
[33] T. Kotani, Phys. Rev. Lett. **74**, 2989 (1995).
[34] T. Kotani and H. Akai, Phys. Rev. B **54**, 16502 (1996).
[35] T. Kotani, Phys. Rev. B **50**, 14816 (1994).
[36] T. Kotani and H. Akai, Phys. Rev. B **52**, 17153 (1995).
[37] Y. Li, J. B. Krieger, M. R. Norman, and G. J. Iafrate, Phys. Rev. B **44**, 10437 (1991).
[38] J. B. Krieger, Y. Li, and G. J. Iafrate, Phys. Rev. A **45**, 101 (1992).
[39] D. M. Bylander and L. Kleinman, Phys. Rev. Lett. **74**, 3660 (1995).
[40] J. B. Krieger, Y. Li, and G. J. Iafrate, Phys. Rev. A **47**, 165 (1993).
[41] J. B. Krieger, Y. Li, and G. J. Iafrate, Phys. Rev. A **46**, 5453 (1992).
[42] D. M. Bylander and L. Kleinman, Phys. Rev. B **52**, 14566 (1995).
[43] D. M. Bylander and L. Kleinman, Phys. Rev. B **54**, 7891 (1996).
[44] D. M. Bylander and L. Kleinman, Phys. Rev. B **55**, 9432 (1997); ibid. **56**, 7022 (1997) (E).
[45] A. Görling and M. Levy, Phys. Rev. A **50**, 196 (1994).
[46] M. Städele, J. A. Majewski, P. Vogl, and A. Görling, Phys. Rev. Lett. **79**, 2089 (1997).
[47] A. Görling, Phys. Rev. Lett. **83**, 5459 (1999).
[48] S. Ivanov, S. Hirata, and R. J. Bartlett, Phys. Rev. Lett. **83**, 5455 (1999).
[49] S. Kümmel and J. P. Perdew, Phys. Rev. Lett. **90**, 043004 (2003).
[50] S. Kümmel and J. P. Perdew, Phys. Rev. B **68**, 035103 (2003).
[51] A. Görling, Phys. Rev. B **53**, 7024 (1996).
[52] M. S. Hybertsen and S. G. Louie, Phys. Rev. B **35**, 5585 (1987).
[53] C. Filippi, X. Gonze, and C. J. Umrigar, in: Recent Developments and Applications of Density Functional Theory, edited by J. M. Seminario, (Elsevier, Amsterdam, 1996), and references therein.
[54] C.-O. Almbladh and U. von Barth, Phys. Rev. B **31**, 3231 (1985).
[55] N. Troullier and J. L. Martins, Phys. Rev. B **43**, 1993 (1991).
[56] M. Moukara, M. Städele, J. A. Majewski, P. Vogl, and A. Görling, J. Phys.: Condens. Matt. **12**, 6783 (2000).
[57] A. Höck and E. Engel, Phys. Rev. A **58**, 3578 (1998).
[58] B. A. Shadwick, J. D. Talman, and M. R. Norman, Comput. Phys. Commun. **54**, 95 (1989).
[59] T. Kreibich, E. K. U. Gross, and E. Engel, Phys. Rev. A **57**, 138 (1998).
[60] E. Engel and R. M. Dreizler, Density Functional Theory II, edited by R. F. Nalewajski (Berlin: Springer, 1996); E. Engel, H. Müller, C. Speicher, and R. M. Dreizler, Density Functional Theory, edited by E. K. U. Gross and R. M. Dreizler (New York: Plenum Press,1995).
[61] C. F. Malius and W. A. Goddard III, Phys. Rev. B **10**, 1528 (1974).
A. Redondo, W. A. Goddard III, and T. C. McGill, Phys. Rev. B **15**, 5038 (1977).
[62] P. A. Christiansen, Y. S. Lee, and K. S. Pitzer, J. Chem. Phys. **71**, 4445 (1979).
[63] L. R. Kahn, P. Baybutt, and D. G. Truhlar, J. Chem. Phys. **65**, 3826, (1976).
[64] J. P. Perdew and A. Zunger, Phys. Rev. B **23**, 5048 (1981).
[65] S. G. Louie, S. Froyen, and M. L. Cohen, Phys. Rev. B **26**, 1738 (1982).
[66] S. Kalvoda, B. Paulus, P. Fulde, and H. Stoll, Phys. Rev. B **55**, 4027 (1997).
[67] S. Strite, J. Ruan, Z. Li, N. Manning, A. Salvador, H. Chen, D. J. Smith, W. J. Choyke, and H. Morkoç, J. Vac. Sci. Technol. B **9**, 1924 (1991).
[68] M. Causa, R. Dovesi, and C. Roetti, Phys. Rev. B **43**, 11937 (1991).
[69] M. Palummo, C. M. Bertoni, L. Reining, and F. Finocchi, Physica B **185**, 404 (1993).
[70] CRC Handbook of Chemistry and Physics, 73rd ed., edited by D. R. Lide (Chemical Rubber Company, Boca Raton, 1992).
[71] S. Massidda, M. Posternak, and A. Baldereschi, Phys. Rev. B **48**, 5058 (1993), and references therein.
[72] A. Mainwood, in Properties and Growth of Diamond, edited by G. Davies (Electronic Materials Information Service, London, 1994), p. 3.
[73] W. R. L. Lambrecht, B. Segall, M. Suttrop, M. Yoganathan, R. P. Devathy, W. J. Choyke, J. A. Edmond, J. A. Powell, and M. Alouani, Appl. Phys. Lett. **63**, 2747 (1993); Phys. Rev. B **50**, 10 722 (1994).

© 2004 WILEY-VCH Verlag GmbH & Co. KGaA, Weinheim

[74] G. Ramirez-Flores, H. Navarro-Contreras, A. Lastras-Martinez, R. C. Powell, and J. E. Greene, Phys. Rev. B **50**, 8433 (1994).
[75] E. Shirley, X. Zhu, and S. G. Louie, Phys. Rev. B **56**, 6648 (1997).
[76] R. W. Godby, M. Schlüter, and L. J. Sham, Phys. Rev. B **37**, 10159 (1988).
[77] X. Zhu, M. S. Hybertsen, and S. G. Louie, in: Atomic-Scale Calculations of Structures in Materials, edited by M. S. Dowe and M. Schlüter, MRS Symposia Proceedings No. 193 (Materials Research Society, Pittsburgh, 1990), p. 113.
[78] V. Fiorentini, Phys. Rev. B **46**, 2086 (1992).
[79] G. Dresselhaus, A. F. Kip, and C. Kittel, Phys. Rev. **98**, 368 (1955).
[80] V. I. Gavrilenko and F. Bechstedt, Phys. Rev. B **55**, 4343 (1997).
[81] B. Adolph, V. I. Gavrilenko, K. Tenelsen, F. Bechstedt, and R. Del Sole, Phys. Rev. B **53**, 9797 (1996).
[82] R. Del Sole and R. Girlanda, Phys. Rev. B **48**, 11789 (1993).
[83] M. Alouani, L. Brey, and N. E. Christensen, Phys. Rev. B **37**, 1167 (1988).
[84] P. Lautenschlager, M. Garriga, S. Logothetidis, and M. Cardona, Phys. Rev. B **35**, 9174 (1987), and references therein.
[85] W. G. Aulbur, M. Städele, and A. Görling, Phys. Rev. B **62**, 7121 (2000).
[86] A. Fleszar, Phys. Rev. B **64**, 245204 (2001).
[87] M. S. Hybertsen and S. G. Louie, Phys. Rev. B **34**, 2920 (1986).
[88] L. Kleinman and D. M. Bylander, Phys. Rev. Lett. **48**, 1425 (1982).
[89] L. Kleinman, Phys. Rev. B **21**, 2630 (1980).
[90] D. M. Bylander and L. Kleinman, Phys. Rev. B **29**, 1534 (1984).
[91] S. L. Chuang and C. S. Chang, Phys. Rev. B **54**, 2491 (1996).
[92] J. A. Majewski, M. Städele, and P. Vogl, MRS Internet J. Nitride Semicond. Res. **1**, 30 (1996).
[93] J. A. Majewski, M. Städele, and P. Vogl, Mat. Res. Soc. Symp. Proc. **449**, 887 (1997).
[94] D. Volm, K. Oettinger, T. Streibl, D. Kovalev, M. Ben-Chorin, J. Diener, B. K. Meyer, J. Majewski, L. Eckey, A. Hoffmann, H. Amano, K. Hiramatsu, and D. Detchprohm, Phys. Rev. B **53**, 16543 (1996).
[95] S. Chichibu, A. Shikanai, T. Azuhata, T. Sota, A. Kuramata, K. Horino, and S. Nakamura, Appl. Phys. Lett. **68**, 3766 (1996).
[96] J. Li, K. B. Nam, M. L. Nakarmi, J. Y. Lin, H. X. Jiang, P. Carrier, and Su-Huai Wei, Appl. Phys. Lett. **83**, 5163 (2003).
[97] R. Dingle, D. D. Sell, S. E. Stokowski, and M. Ilegems, Phys. Rev. B **4**, 1211 (1971).
[98] G. Dresselhaus, Phys. Rev. **186**, 824 (1958).
[99] M. Cardona, N. E. Christensen, and G. Fasol, Phys. Rev. B **38**, 1806 (1988).
[100] N. E. Christensen and M. Cardona, Solid State Commun. **51**, 491 (1984).
[101] G. Dresselhaus, Phys. Rev. **100**, 580 (1955).
[102] G. L. Bir and G. E. Pikus, Symmetry and Strain-Induced Effects in Semiconductors (Wiley, New York, 1974).
[103] J. M. Luttinger and W. Kohn, Phys. Rev. **97**, 869 (1955).
J. M. Luttinger, **102**, 1030 (1956).
[104] M. B. Burt, Phys. Rev. B **50**, 7518 (1994); J. Phys. Condens. Matter **4**, 6651 (1992).
[105] B. A. Foreman, Phys. Rev. B **52**, 12241 (1995).
[106] Lin-Wang Wang and Alex Zunger, Phys. Rev. B **54**, 11417 (1996).
[107] S. de Franceschi, J.-M. Jancu, and F. Beltram, Phys. Rev. B **59**, 9691 (1999).
[108] M. Sabathil, S. Hackenbuchner, J. A. Majewski, G. Zandler, and P. Vogl, Journal of Computational Electronics **1**, 81 (2002).
[109] S. Hackenbuchner, M. Sabathil, J. A. Majewski, G. Zandler, P. Vogl, E. Beham, A. Zrenner, and P. Lugli, Physica B **314**, 145–149 (2002).
[110] The software package is freely available on http://www.wsi.tum.de/nextnano3.
[111] See, e.g., Proc. of the 7th Int. Workshop on Computational Electronics, Glasgow, Scotland, May 22–25, 2000 and papers therein.
[112] A. Kumar, S. E. Laux, and F. Stern, Phys. Rev. B **42**, 5166 (1990).
S. E. Laux, in: Proc. 5th Int. Conf. on Numerical Analysis of Semiconductor Devices and Integrated Circuits (NASECODE V), ed. J. J. H. Miller (Boole, Dun Laoghaire, Ireland, 1987), pp. 270–275.
[113] M. Grundmann, O. Stier, and D. Bimberg, Phys. Rev. B **59**, 5688 (1999).
[114] C. Pryor, Phys. Rev. B **57**, 7190 (1998); ibid., B **60**, 2869 (1999).
[115] M. A. Cusack, P. R. Briddon, and M. Jaros, Phys. Rev. B **54**, R2300 (1996).
[116] C. Pryor, J. Kim, L. W. Wang, A. J. Williamson, and A. Zunger, J. Appl. Phys. **83**, 2548 (1998).

© 2004 WILEY-VCH Verlag GmbH & Co. KGaA, Weinheim

[117] F. Findeis, M. Baier, E. Beham, A. Zrenner, and G. Abstreiter, Appl. Phys. Lett. **78**, 2958 (2001).
[118] C. Van de Walle, Phys. Rev. B **39**, 1871 (1989).
[119] M. V. Fischetti, Phys. Rev. B **59**, 4901 (1999).
[120] M. Grundmann, O. Stier, and D. Bimberg, Phys. Rev. B **52**, 11969 (1995).
[121] S. Selberherr, Analysis and Simulation of Semiconductor Devices (Springer, Wien, 1984).
[122] C. S. Lent and D. J. Kirkner, J. Appl. Phys. **67**, 6353 (1990).
[123] W. R. Frensley, Superlattices and Microstructures **11**, 347 (1992).
[124] Z. Bai, J. Demmel, J. Dongarra, A. Ruhe, and H. van der Vorst, Editors, Templates for the Solution of Algebraic Eigenvalue Problems, (SIAM, Philadelphia, 2000).
[125] A. Trellakis, A. T. Galick, A. Pacelli, and U. Ravaioli, J. Appl. Phys. **81**, 7880 (1997).
[126] J. R. Downes, D. A. Faux, and E. P. O'Reilly, J. Appl. Phys. **81**, 6700 (1997).
[127] P. W. Fry, I. E. Itskevich, D. J. Mowbray et al., Phys. Rev. Lett. **84**, 733 (2000).
[128] P. W. Fry, D. J. Mowbray, I. E. Itskevich, et al., phys. stat. sol. (b) **224**, No. 2, 497 (2001).
[129] A. J. Williamson, L. W. Wang, and A. Zunger, Phys. Rev. B **62**, 12963 (2000).
[130] N. Liu, J. Tersoff, O. Baklenov, et al., Phys. Rev. Lett. **84**, 334 (2000).
[131] G. Czajkowski, F. Bassani, L. Silvestri, phys. stat. sol. (a) **188**, 1281 (2001).
[132] R. J. Warburton, C. Schulhauser, D. Haft, et al., Phys. Rev. B **65**, 113303/1 (2002).
[133] J. El Khamkhami, E. Feddi, E. Assaid, et al., Physics of Low-Dimensional Structures **131** (2001).
[134] J. Seufert, M. Obert, M. Scheibner, et al., Appl. Phys. Lett. **79**, 1033 (2001).
[135] W. H. Chang, T. M. Tsu, C. C. Huang, et al., Phys. Rev. B **62**, 6959 (2000).
[136] M. Pacheco and Z. Barticevic, Phys. Rev. B **64**, 033406/1 (2001).

© 2004 WILEY-VCH Verlag GmbH & Co. KGaA, Weinheim